TITLE: The embryonic zebrafish brain is seeded by a lymphatic-dependent population of *mrc1*$^{+}$ microglia precursors

AUTHOR LIST: *Lauren A. Green[1,2], *Michael[1], Caroline A. Hoover[1,2], Dana F. DeSantis[1,2], and Cody J. Smith[1,2]

* The authors contributed equally

AFFILIATIONS: Department of Biological Sciences[1] and The Center for Stem Cells and Regenerative Medicine[2] at the University of Notre Dame, Notre Dame, IN.

CORRESPONDING AUTHOR:

Cody J. Smith, PhD

Department of Biological Sciences

University of Notre Dame

015 Galvin Life Sciences Building

Notre Dame, IN 46556

Email: csmith67@nd.edu

Phone: 574-631-3959

ABSTRACT:

Microglia are the resident macrophages of the central nervous system that serve critical roles in brain construction. Although human brains contain microglia by 4 weeks gestation, an understanding of the earliest microglia that seed the brain during its development remains unresolved. Using timelapse imaging in zebrafish, we discovered a *mrc1a*$^{+}$ microglia precursor population that seeds the brain before traditionally described microglia. These early microglia precursors are dependent on lymphatic vasculature that surrounds the brain and are independent of *pu1*$^{+}$ yolk sac-derived microglia. Single-cell RNA sequencing datasets reveal *Mrc1*$^{+}$ microglia in the embryonic brain of mice and humans. We then show in zebrafish that these early *mrc1a*$^{+}$ microglia precursors preferentially expand during pathophysiological states in development. Taken together, our results identify a critical role of lymphatics in the microglia precursors that seed the early embryonic brain.

MAIN TEXT

INTRODUCTION:

Microglia have substantial roles in brain construction[1–9]. We know microglia precursors can be detected in the human embryonic brain as early as 4 weeks gestation[10–13], before peak stages of neurogenesis, gliogenesis and synaptogenesis[14]. Colonization is believed to occur over several weeks in humans, with peak microglia density reached around 20 weeks[15]. Microglia colonize the mouse around E9.5 with significant expansion by E10.5[16]. We know fate mapping with tamoxifen-inducible Runx1-Cre mice activated at E7.5 demonstrates labeling of 30% of microglia at E10.5[16]. In zebrafish, we also know the yolk sac generates microglia precursors that seed the brain in early development between 2-3 dpf (days post-fertilization), although L-plastin$^+$ cells can be identified at 35 hpf[17,18]. Studies in mice and zebrafish support the hypothesis that microglia may also have additional sources besides the yolk sac[19–22]. Still, relatively little is known about the first microglia, or pioneer microglia, to colonize the embryonic brain.

Here we utilize timelapse imaging to show a population of *mrc1a*$^+$ microglia-like cells that colonizes the embryonic zebrafish brain before traditionally described *pu1*$^+$ microglia populations and prior to peak stages of synaptic and glia genesis. Analysis of scRNA sequencing datasets from both mouse and human fetal tissue demonstrate mammalian embryonic microglia also express MRC1/*Mrc1.* We show *mrc1a*$^+$ microglia precursors develop independently of the traditional *pu1*$^+$ yolk sac-derived microglia lineage in zebrafish. Intravital imaging revealed that *mrc1a*$^+$ cells within and associated with lymphatic vessels that surround the brain, leave the vessels and colonize the brain.

Colonization of *mrc1a*$^+$ microglia in zebrafish is reduced with multiple manipulations that disrupt lymphangiogenesis. Finally, we show *mrc1a*$^+$ microglia are the primary responding microglia population during a developmental injury. Together, these data implicate brain-border lymphatic vessels as central to the early colonization of microglia precursors.

RESULTS:

Microglia-like cells express *mrc1a*

To explore embryonic microglia, we initially scored the abundance of microglia in the 5 dpf zebrafish brain. To do this we used the 4C4 antibody which specifically labels microglia in zebrafish[23]. We then co-localized 4C4 with *Tg(pu1:Gal4;UAS:gfp)* which labels yolk sac-derived microglia/macrophage populations[24]. This analysis identified that 36.5 ± 0.226% of zebrafish microglia could be labeled by the *pu1* transgene. 4C4 also marked 28.1% of Eos$^+$ cells from *Tg(pu1:eos)* animals, consistent with the idea that *Tg(pu1:Gal4;UAS:gfp)* animals were marking the portion of 4C4$^+$ cells that were also *pu1*$^+$ (Extended Data Figure 1A).

To next explore the possibility that additional embryonic populations label or contribute to the pool of microglia, we screened transgenes labeling major cell types and lineages in the brain or periphery, including oligodendrocyte lineage cells or neural crest (*sox10)*, neurons (*neurod),* lymphocytes (*lck*), vasculature (*fli1a)*, and venous vasculature/lymphatics (*mrc1a)*[25]*.* We did not detect 4C4 immunolabeling in *sox10, neurod, lck,* or *fli1a* cells. In contrast, *mrc1a* labeled 82.99 ±0.069% of 4C4$^+$ cells in the brain (Figure 1A-1B), indicating a potential contribution of *mrc1a*$^+$ cells to the embryonic

microglia pool. For simplicity's sake, below we will refer to cells in the *Tg(mrc1a:egfp)* to GFP animals as *mrc1a*$^{+}$.

Microglia are located throughout the CNS, so we next quantified whether *mrc1a*$^{+}$;4C4^{+} cells are present across various CNS regions. To do this we imaged the brain, hindbrain, and spinal cord of *Tg(mrc1a:egfp);Tg(gfap:nfsb-mCherry)* animals, stained with 4C4, and scored the abundance of *mrc1a*$^{+}$;4C4^{+} cells in each CNS region (Figure 1C-1D). Co-labeled cells were located in all areas of the CNS. We confirmed this localization with a second transgenic line that marked the parenchyma with a panneuronal-expressing *dsred*, *Tg(mrc1a:egfp);Tg(nbt:dsred)* (Extended Data Figure 1B-1E). Unlike vessel associated cell populations like brain lymphatic endothelial cells, FGPs, and brain-border macrophages that would be expected to interact with vessels outside of the CNS parenchyma[26–28], *mrc1a*$^{+}$;4C4^{+} cells were located within the CNS proper (Figure 1C-1D). We further confirmed that these *mrc1a*$^{+}$ cells in the parenchyma are separate and distinguishable from stationary lymphatic vessel endothelium by timelapse imaging motile *mrc1a*$^{+}$ cells in the embryonic brain (Supplementary Video 1). They are also present in the spinal cord, where FGP cells (which also label with *mrc1a*) are not present (Figure 1C-1D)[27]. These data are consistent with the hypothesis that *mrc1a*$^{+}$ cells may represent a microglia-like precursor population that seeds the embryonic brain.

We would expect microglia or their precursors to be labeled with *apoeb* and L-plastin (Lcp1)[29]. Therefore, we first stained *Tg(mrc1a:egfp)* animals at 5 dpf with Lcp1 and 4C4. In this analysis, we identified *mrc1a*$^{+}$;Lcp1^{+};4C4^{+} cells in the zebrafish brain (Figure 1E-

1F, Extended Data Figure 1F-1G). In situ hybridization demonstrated that *mrc1a*$^{+}$ cells in the parenchyma also expressed *apoeb*. (Figure 1E-F, Extended Data Figure 1C). We also tested if they were marked by *lyve1b*, Flt4, or Prox1, which are expressed in vascular endothelial populations (Figure 1E-F; Extended Data Figures 1F-G)[25,30,31]. However, *mrc1a*$^{+}$ cells in the parenchyma did not label with those markers (Figure 1E-F; Extended Data Figure 1C). These data are consistent with the hypothesis that a *mrc1a*$^{+}$ microglia population seeds the zebrafish embryonic brain.

To determine if this is a transient population that is present only during embryogenesis, we scored the abundance of *mrc1a*$^{+}$*;*4C4^{+} cells in *Tg(mrc1a:egfp)* brains at 7 and 15 dpf (Figure 1G-1I). Most microglia at both time points are only labeled with 4C4. However, *mrc1a*$^{+}$*;*4C4^{+} microglia could also be detected at 7 and 15 dpf and thus persist at least into the juvenile zebrafish brain.

mrc1a^{+} microglia function like traditional microglia

Microglia clear debris in the developing CNS[1–9]. To test if *mrc1a*$^{+}$ microglia also clear parenchymal debris, we used 5 dpf *Tg(mrc1a:egfp)* animals immunostained with 4C4 and a combination of transgenic animals and antibody staining to label synaptic (synapsin, SV2, and znp-1), neuronal (acetylated tubulin, *nbt*), oligodendrocyte lineage cell (*sox10)*, astroglial (*GFAP*), and microglia (*pu1*) debris. We used IMARIS to confirm and visualize the engulfment of labeled debris by *mrc1a*$^{+}$ microglia(Figure 2A, Extended Data Figure 2A). This revealed that *mrc1a*$^{+}$ microglia phagocytose most neural debris in the developing CNS (Figure 2B). *mrc1a*$^{+}$ cells contained debris in higher proportions than

pu1$^+$ microglia for some types of debris (Figure 2C, Extended Data Figure 2B). Thus like typical microglia, *mrc1a*$^+$ microglia clear multiple types of debris in the parenchyma.

We next asked if *mrc1a*$^+$ microglia migrate like traditional microglia by tracking individual microglia labeled with *pu1* and *mrc1a* across three imaging regions in the CNS from 4 dpf to 5 dpf. We did not observe a difference in the average speed or total distance traveled by migrating microglia regardless of their *pu1*$^+$ or *mrc1a*$^+$ identity (Figure 2D,E). Previous work shows homotypic microglia-microglia interactions are repulsive while macrophage-microglia interactions are not repulsive[32]. To test whether *mrc1a*$^+$ microglia also exhibit repulsion following interactions with other microglia, we tracked *pu1*$^+$ and *mrc1a*$^+$ microglia throughout three 0.0027 mm^3 imaging windows for 24 hours and observed three unique microglia interactions: *pu1-pu1*, *mrc1a-mrc1a*, and *mrc1a-pu1*. Each interaction resulted in contact-dependent repulsion (Figure 2F-2H; Extended Data Figures 2C-2E), consistent with a microglia identity of the *mrc1a*$^+$ cells.

Mrc1a$^+$ cells colonize the brain early in development

Microglia populations can be identified in the human brain as early as 4 weeks gestation[14]. To ask whether *mrc1a*$^+$ microglia might contribute to pioneer microglia-like cells, we explored the earliest seeding of microglia precursors in the brain. We compared this to *pu1*$^+$ and *mpeg1*$^+$ cells, traditional markers for microglia precursors that seed the zebrafish brain at 2 to 3 dpf[18–20]. To explore this, we imaged *Tg(mrc1a:egfp); Tg(pu1:Gal4;UAS:rfp)* and *Tg(mrc1a:egfp); Tg(mpeg1:mCherry)* in the zebrafish brain at 36 hpf and 48 hpf. Such ages correspond with the neurogenesis stages where human

microglia can first be identified. We fixed and stained these animals with GFAP to mark the CNS radial glial boundary and confirm a cell was present within the brain parenchyma and away from the *mrc1a*$^{+}$ lymphatic/venous vessels that surrounded the brain (Figure 3A-3E). We could not detect *pu1*$^{+}$ or *mpeg1*$^{+}$ cells present in the brain at 36 hpf. An average of 0.429 ± 0.202 *pu1*$^{+}$ and 0.444 ± 0.242 *mpeg1*$^{+}$ cells were present in the brain imaging window at 48 hpf, consistent with previous reports that *pu1*$^{+}$ precursors seed the brain after 2 dpf (Figure 3F)[18]. In contrast, an average of 1.077 ± 0.211 *mrc1a*$^{+}$ cells were present within the brain imaging window at 36 hpf and *mrc1a*$^{+}$ cells were more abundant in the brain at 48 hpf, with higher relative abundance than *pu1*$^{+}$ and *mpeg*$^{+}$ cells. Cells that label with both *mrc1a*$^{+}$;4C4^{+} were detected at 48 hpf, consistent with the hypothesis that the early *mrc1a*$^{+}$ cells persist throughout the embryonic brain (Figure 3F). We could not detect any 4C4^{+} cells at 48 hpf that also label with *pu1* or *mpeg1*.

Microglia in the mammalian embryonic brain express Mrc1

We next examined the transcriptomes of murine microglia in early development using previously published single-cell RNA sequencing data to determine if *Mrc1* is expressed in mammalian microglia precursors, in addition to the expression that has already been described in border-associated macrophages (BAMs)[29,33](Figure 4A). We first analyzed approximately 70,000 transcriptomes of microglia and macrophages from E14.5, P4/5, and P30 mice. E14.5 captures embryonic microglia and P4/P5 captures post-embryonic, early-juvenile microglia ages that would correspond with the myelination states that are present in 5 dpf zebrafish when we can detect *mrc1a*$^{+}$ microglia-like cells. P30 mice were included for an adult reference. We utilized hierarchical clustering to remove

contaminating neurons and endothelial cells, and then re-clustered the remaining cells (Extended Data Figure 3A-B), which revealed 16 distinct clusters (Figure 4B; Extended Data Figure 3C). While cluster 3 expressed neuronal markers , the remaining clusters all expressed macrophage genes (Figure 4B; Extended Data Figure 3C). To determine whether these clusters were composed of microglia or BAMs, we created sets of marker genes which were differentially expressed in microglia and BAMs in published RNA-sequencing data from embryonic mice[34]. We then examined expression of these gene sets across the 15 macrophage clusters. Cluster 2 exhibited notably higher expression of genes in the BAM gene set –such as *Mrc1, F13a1*, *Lyve1*, and *Cd163* –compared to all other clusters (Figure 4C). The fourteen other clusters expressed genes in the microglia gene set –such as *Tmem119*, *P2ry12*, and *Hexb*[35–38,40] –more highly than Cluster 2 cells (Figure 4C). Based on expression of the two gene sets, we classified Cluster 2 as BAMs and the remaining clusters as microglia. Several of these clusters replicated previously described subtypes[29], including an *Ms4a7*$^{+}$ cluster highly enriched in *Mrc1* (Cluster 10), which was most highly prevalent at E14.5 compared to later ages, supporting the hypothesis that *Mrc1* may label a subset of embryonic microglia in mammals (Figure 4C & E). Interestingly, we observed 11.6% of the cells in the fourteen microglia clusters expressed detectable *Mrc1.* To determine whether these *Mrc1*$^{+}$ cells were microglia-like and not BAMs, we examined expression of the microglia and BAM gene sets between *Mrc1*$^{+}$ and *Mrc1*$^{-}$ cells from the 14 putative microglia clusters, including Cluster 2 cells as a reference for BAMs (Figure 4D). We find that the *Mrc1*$^{+}$ cells exhibited minimal differences in expression of these gene sets compared to the *Mrc1*$^{-}$ cells (Figure 4D; Supplementary Table 1). We further found that *Mrc1*$^{+}$ microglia exhibit higher enrichment

of the microglia gene set and lower enrichment of the BAM gene set than Cluster 2 BAMs. The small differences in microglia gene expression are likely due to developmental age, as *Mrc1*$^{+}$ microglia were more highly prevalent in younger animals (E14.5 and P4-5) and were markedly reduced at P30 (Figure 4E).

We next asked whether *MRC1*-expressing microglia are present in human development by exploring a dataset of over 13,000 microglia from human fetal tissue[33] (Figure 4A). Using hierarchical clustering, we first removed contaminating populations of neurons and erythrocytes, and then re-clustered the remaining cells, yielding 10 final clusters (Extended Data Figure 3E-F). One of these clusters (Cluster 8), was enriched in leukocyte genes like *S100A9* and *LILRA5*, while the other clusters expressed typical macrophage genes (Extended Data Figure 3G; Supplementary Table 1). Examining microglia versus BAM gene sets showed Cluster 9 exhibited the highest expression of BAM genes and the lowest expression of microglia genes (Figure 4G). The remaining clusters more highly expressed the microglia gene set and did not display notable enrichment of the BAM gene set. Clusters 3 & 10 exhibited lower expression of microglia genes but also minimal enrichment of BAM genes, which may indicate these cells are less mature microglia. We further discovered that, of the 13,430 cells in the potential microglia clusters, 8.6% expressed *MRC1*. The *MRC1*$^{+}$ cells expressed the microglia gene set more highly and the BAM gene set lower than Cluster 2 BAMs, and expressed both these gene sets comparably to *MRC1*$^{-}$ microglia (Figure 4H; Supplementary Table 1). We thus conclude that these *MRC1*$^{+}$ cells are indeed microglia. Like the mouse scRNA sequencing analysis, Spi1/Pu.1 was detected in a portion of both *MRC1*$^{+}$ and *MRC1*$^{-}$ microglia (Extended Data

Figure 3D,H). Although microglia in both mice and humans express *Mrc1*/*MRC1* during development, further work will be needed to confirm the existence of these populations in mammals, and to determine whether this population shares other characteristics with the embryonic zebrafish microglia.

mrc1a^{+} microglia are dependent on lymphangiogenesis

We next explored the developmental ontogeny of *mrc1a*$^{+}$ microglia in zebrafish. In addition to expression in parenchyma-located microglia, *mrc1a/Mrc1* is expressed in lymphatic and venous vessels, brain-border macrophages, FGPs and brain lymphatic endothelial cells (BLECs)[26,27,39]. These *mrc1a*$^{+}$ vessels surrounding the brain uptake Qdot705 when it is injected into the head, consistent with their classification as lymphatic vasculature[26]. Light sheet microscopy revealed that lymphatic vessels surround the brain in the embryo, right outside the *gfap*$^{+}$ boundary (Figure 5A-5B). To investigate the potential role of these embryonic brain-border lymphatic vessels in *mrc1a*$^{+}$ microglia, we timelapsed the brain-border *mrc1a*$^{+}$ vessel in the anterior region of the head and its surrounding brain region for 24 hrs. Orthogonal rotations of these images demonstrate a luminal space in the center of the vessel (Figure 5C). In timelapse movies, we noted two observations that showed an interaction with migratory *mrc1a*$^{+}$ cells and *mrc1a*$^{+}$ lymphatic vessels. First, *mrc1a*$^{+}$ cells could be seen migrating along and circling *mrc1a*$^{+}$ lymphatic vessels (Figure 5D-5E, Supplementary Video 1). We also identified *mrc1a*$^{+}$ cells within the *mrc1a*$^{+}$ lymphatic vessels that extended processes outside of the vessel and then eventually exited the vessel (Supplementary Video 2,3). Rotational images in IMARIS confirmed the intra-vessel location throughout the movie. While exiting, they displayed an

hourglass shape, indicative of cells leaving confined barriers[32,40]. These migratory *mrc1a*$^{+}$ vessels then traveled away from the vessel, unlike FGP cells that remain associated or close to the lymphatic vessels. Together these data are consistent with the possibility that *mrc1a*$^{+}$ microglia precursors could utilize the lymphatic vessels for brain colonization, placing the brain-border lymphatics as central to embryonic microglia colonization.

Therefore, we next asked if *mrc1a*$^{+}$ microglia colonization was dependent on lymphatic vessels. To test this, we first replicated a drug screen that revealed small molecules that impede lymphangiogenesis[41]. *Tg(mrc1a:egfp);Tg(gfap:nfsb-mCherry)* animals were dosed with individual inhibitors daily from 48 hpf to 120 hpf and fixed and immunostained with 4C4 at 120 hpf. We confirmed inhibition of lymphangiogenesis by measuring the average length and number of lymphatic vessels and secondary sprouts (Extended Data Figures 4A-4F). To determine whether *mrc1a*$^{+}$ microglia are dependent on lymphatic vessels, we next quantified the average percentage of 4C4^{+} microglia which were *mrc1a*$^{+}$. We observed a significant reduction in the number of microglia in the brain which were *mrc1a*$^{+}$ across the lymphatic inhibitor treatment groups compared to DMSO (Figure 5F-5G), consistent with the hypothesis that *mrc1a*$^{+}$ microglia could be dependent on lymphangiogenesis.

As a complementary approach, we also inhibited lymphatic vessel formation genetically using two *flt4* sgRNAs. *Flt4* is required for the production of lymphatic vessels[25,28,42]. We first confirmed that injection of *flt4* sgRNA/Cas9 reduced the lymphatic vessels in *Tg(mrc1a:egfp)* animals, but not in Cas9 only or uninjected controls(Figure 6A). With

T7E1 we identified that the animals with perturbed lymphatic vessels had indels at the *flt4* locus. To determine if *mrc1a*$^{+}$ microglia were reduced after *flt4* sgRNA injection, *mrc1a*$^{+}$ cells in the parenchyma were immunostained with 4C4 . We noted that *mrc1a*$^{+}$*;*4C4^{+} cells were reduced after injection with *flt4* sgRNA (Figure 6B-6C, Extended Data Figures 5A-5B). These injections did not reduce the number of 4C4^{+} only cells in the brain or those that were labeled with only *mrc1a*. Although it remains a possibility that *mrc1a*$^{+}$ microglia require *flt4* for differentiation, together these results with the pharmacological manipulations of lymphatic vessels are most consistent with the hypothesis that *mrc1a*$^{+}$*;*4C4^{+} microglia are dependent on lymphatic vessels.

We next asked more specifically if lymphatic endothelial vessels or cells around or in the brain are required for colonization of *mrc1a*$^{+}$ microglia precursors. To test this, we disrupted *mrc1a*$^{+}$ endothelial cells in and around the brain with Verteporfin at 24 hpf, 12 hours before we initially visualize *mrc1a*$^{+}$ cell migration from lymphatic vessels, and then scored the number of free-roaming *mrc1a*$^{+}$ cells in the brain at 4 dpf (Figure 6D-6H). Verteporfin is a photodynamic drug that when exposed to 640 nm light causes specific perturbation of lymphatic endothelial cells, thereby providing precise spatiotemporal control of the perturbation[43,44]. As a control, we exposed animals to 1 μM verteporfin but not 640 nm light. We first confirmed via timelapse imaging that the exposure to Verteporfin and 640 nm light caused *mrc1a*$^{+}$ lymphatic vessels outside the brain to swell and degrade by 3.21±1.32 hours post 640 nm exposure (n=4 animals) (Figure 6G-6H). Three days post treatment, Verteporfin-treated animals exposed to 640 nm in the head exhibited less *mrc1a*$^{+}$ cells in the brain (1.25 cells on average in the parenchyma per 0.0027 mm^{3}

imaging window) compared to non-photoactivated control animals (on average 8.75 *mrc1a*$^{+}$ cells; p=0.0042; Figure 6E-6F). These data support the hypothesis that *mrc1a*$^{+}$ microglia may be dependent on brain-border lymphatic endothelial vessels or cells.

Our data supports the hypothesis that *mrc1a*$^{+}$ microglia colonize the brain at a distinct time from *pu1*$^{+}$ microglia (Figure 2F). To ask if these *pu1*$^{+}$ microglia also utilize lymphatics distinctly to colonize the brain, we repeated two of the lymphatic inhibitor treatments with strong reduction in the *mrc1a*$^{+}$ microglia (Figure 5D-5E), in *Tg(pu1:Gal4;UAS:gfp); Tg(gfap:nfsb-mCherry)* animals immunostained with 4C4. The number of *pu1*$^{+}$ cells did not change upon treatment with leflunomide and flunarizine compared to DMSO-treated animals (Extended Data Figure 4G-4I), consistent with the hypothesis that brain lymphatics have a role in *mrc1a*$^{+}$ microglia colonization –a role that is not shared with *pu1*$^{+}$ yolk sac-derived microglia.

Traditional *pu1*$^{+}$ microglia migrate from the rostral blood islands (RBI) in the yolk sac to the brain[16,19]. To narrow the potential direct source of *mrc1a*$^{+}$ microglia, we fate-mapped cells with the photoconvertible fluorescent protein, Eos. In this paradigm, *bactin:eos* was injected into *Tg(mrc1a:egfp)* at the one-cell stage, photoconverted with a diffraction-limited laser in specific regions of interest at 24 hpf, grown for 24 hours post-conversation and then fixed for anti-GFP staining (Figure 6I). Photoconversion of Eos in the yolk sac at 24 hpf, resulted in few *mrc1a*$^{+}$;p-Eos^{+} cells in the brain at 48 hpf, although we could detect *mrc1a*$^{+}$ cells and *p-Eos*$^{+}$ cells in the brain (Figure 6J-6L). Photoconversion of the RBI at 24 hpf also did not produce *mrc1a*$^{+}$;p-Eos^{+} cells in the brain at 48 hpf. These results

are inconsistent with the hypothesis that the yolk sac or RBI directly produces the majority of the *mrc1a*$^{+}$ cells that are located in the parenchyma. Given that *mrc1a*$^{+}$ microglia are reduced following perturbation of brain-border lymphatics, we next tested if precursor cells in the head at 24 hpf produced *mrc1a*$^{+}$ microglia by photoconverting Eos in the entirety of the head. At 48 hpf, we scored *mrc1a*$^{+}$;pEos^{+} cells in the brain in 75% of the animals (Figure 6J-6L, Extended Data Figures 5C-5D). While it is still possible that *mrc1a*$^{+}$ microglia are derived at some point from other sources, these data support the hypothesis that *mrc1a*$^{+}$ microglia at 48 hpf originate from cells that were present in the head at 24 hpf.

mrc1a^{+} microglia are distinct from *pu1*$^{+}$ microglia

We next sought to address if *mrc1a*$^{+}$ microglia could be further distinguished from traditional *pu1*$^{+}$ microglia. Traditional yolk sac-derived microglia express and are dependent on *pu1 (spi1b)*[19,35]. To determine whether *mrc1a*$^{+}$ microglia are independent of traditionally described yolk sac-derived microglia, we first imaged *Tg(mrc1a:egfp);Tg(pu1:Gal4;UAS:rfp)* animals immunostained with 4C4 at 5 dpf and scored the average number of cells with varying *mrc1a, pu1,* and 4C4 marked expression (Figure 7A). We identified seven marked expression patterns, including small populations of 4C4^{+} only, 4C4^{+};*pu1*$^{+}$*,* and *pu1*$^{+}$;*mrc1a*$^{+}$ cells, and larger populations of *pu1*$^{+}$ only and *mrc1a*$^{+}$ only cells within the CNS imaging window. Most notably, there is an abundant cell population that is *mrc1a*$^{+}$*;*4C4^{+} that does not express *pu1*$^{+}$ (Figure 7B).

To further explore how *mrc1a*$^{+}$ microglia differed from the *pu1*$^{+}$, and *pu1*$^{+}$*;mrc1a*$^{+}$ cells, we assayed their development across embryonic ages from 1-5 dpf in *Tg(mrc1a:egfp); Tg(pu1:Gal4;UAS:rfp)* animals (Extended Data Figures 6A-6G). We also co-stained with 4C4 to identify their mature microglia identity. *mrc1a*$^{+}$ cells in the parenchyma could first be identified at 24 and 36 hpf (Extended Data Figure 6A). The *mrc1a*$^{+}$;4C4^{+} population could first be detected at 2 dpf and expanded after (Extended Data Figure 6D). *pu1*$^{+}$ cells arrived to the brain at 2 dpf, consistent with previous reports of yolk sac-derived microglia populations (Extended Data Figures 6A-6G). As development progressed, so did the populations labeled with 4C4, consistent with the idea that the early seeding of these populations produces a 4C4^{+} mature microglia population (Extended Data Figures 6A-G). To get a precise time of infiltration, we complemented this analysis with timelapse imaging of *Tg(mrc1a:egfp); Tg(pu1:Gal4;UAS:rfp)* animals from 36-56 hpf, a time point which corresponds with the arrival times from the above staining. In these movies, *mrc1a*$^{+}$ cells were first to arrive in the brain, followed by *mrc1a*$^{+}$*;pu1*$^{+}$ and then lastly *pu1*$^{+}$ cells (Figure 7C-7E). Together, these data indicate *mrc1a*$^{+}$ microglia precursors arrive before both the *pu1*$^{+}$ and *mrc1a*$^{+}$*;pu1*$^{+}$ population.

To further investigate how *mrc1a*$^{+}$;4C4^{+} were different from other populations of microglia, we used CRISPR/Cas9 to target the *pu1* genomic locus without disrupting the *pu1* transgenes. We injected the single synthetic-gRNA and Cas9 into *Tg(mrc1a:egfp); Tg(pu1:Gal4;UAS:rfp)* single-cell embryos, fixed and stained with 4C4 and GFAP at 5 dpf, and scored the number of *mrc1a*$^{+}$*, pu1*$^{+}$*,* and 4C4^{+} cells (Figure 7F). Embryos that were not injected were used as controls. The number of cells in all *pu1*$^{+}$ categories was reduced

in crispant animals compared to uninjected animals. These populations include the *pu1*$^{+}$ only, *pu1*$^{+}$;*mrc1a*$^{+}$;4C4^{+}, and *pu1*$^{+}$;*mrc1a*$^{+}$ cell-types (Figure 7G-7J, Extended Data Figure 6H). In contrast, the total number of *mrc1a*$^{+}$ only, and *mrc1a*$^{+}$;4C4^{+}, and 4C4^{+} only cells were not reduced in crispant animals compared to uninjected animals (Figure 7I-7J, Extended Data Figure 6H-6I). Together, these data demonstrate a successful reduction of all *pu1*$^{+}$ populations but not *mrc1a*$^{+}$ cells, again consistent with the hypothesis that *mrc1a*$^{+}$ microglia precursors likely arise independent of *pu1*$^{+}$ microglia.

To determine if *mrc1a*$^{+}$;4C4^{+} were different from other populations of microglia with a second complementary approach, we treated *Tg(mrc1a:egfp); Tg(pu1:Gal4;UAS:rfp)* animals with GW2850, a Csf1r inhibitor, since traditional microglia require Csf1r signaling for development and survival[32,45,46]. Animals were treated from 1 to 5 dpf (Extended Data Figure 6J). We then fixed and immunostained with 4C4 at 5 dpf and quantified that in Csf1r inhibitor-treated animals, the *pu1*$^{+}$ only cells were significantly reduced from an average of 15.8 cells to 3.3 cells per animal (p=0.0015), while the *mrc1a*$^{+}$;4C4^{+} microglia did not change between GW2850-treated (average: 7.8 cells) and DMSO-treated (average: 6.7 cells) animals (p=0.6598; Figure 7K). These data demonstrate that *mrc1a*$^{+}$;4C4 microglia develop independently of *pu1* and are resistant to Csf1r inhibition, again distinct from *pu1*$^{+}$ microglia.

Analysis and manipulations of *mrc1a*$^{+}$;4C4^{+} cells indicated a population of cells that were also *pu1*$^{+}$;*mrc1a*$^{+}$. This *pu1*$^{+}$;*mrc1a*$^{+}$ migrated at an average of 0.486 μm/hr and traveled

287.63 μm, both similarly to *pu1*$^+$ and *mrc1a*$^+$ microglia (*pu1*$^+$*;mrc1a*$^+$ vs. *pu1*$^+$, p=0.999 and *pu1*$^+$*;mrc1a*$^+$ vs *mrc1a*$^+$, p=0.971). We could not test the repulsive nature of the microglia with other microglia because we did not detect contact between *mrc1a*$^+$*;pu1*$^+$ cells and other microglia. Our data indicate that the *pu1*$^+$*;mrc1a*$^+$ population was also reduced by injection of *spi1b* gRNA but not reduced by the Csf1r inhibition (Figure 7K, Extended Data Figure 6H). Further, the *pu1*$^+$*;mrc1a*$^+$ population was present in the brain after the *mrc1a*$^+$ population (Figure 7C-7E). There were three likely hypotheses regarding the *pu1*$^+$*;mrc1a*$^+$ population: 1. a subset *pu1*$^+$ cells from the yolk sac are *mrc1a*$^+$, 2. *mrc1a*$^+$ lymphatic-dependent cells become *pu1*$^+$ and 3. *pu1*$^+$;*mrc1a*$^+$ are a distinct third population. To determine whether the *pu1*$^+$*;mrc1a*$^+$ was related to the *mrc1a*$^+$ population we first injected *flt4* sgRNA into *Tg(mrc1a:egfp); Tg(pu1:Gal4;UAS:rfp)* animals and scored the presence of the *pu1*$^+$*;mrc1a*$^+$ population. These results indicated *pu1*$^+$*;mrc1a*$^+$ or *pu1*$^+$ cells were not reduced (Figure 7L-7M). However, *mrc1a*$^+$*;*4C4$^+$ cells were reduced (Figure 6B) and thus indicated the *pu1*$^+$*;mrc1a*$^+$ is not dependent on lymphatics. Further, if *mrc1a*$^+$ cells upregulate *pu1*, we may expect to see *mrc1a*$^+$ cells in timelapse movies become RFP$^+$ in *Tg(mrc1a:egfp); Tg(pu1:Gal4;UAS:rfp)* animals. However, we were not able to detect the cells transition to label as *pu1*$^+$*;mrc1a*$^+$. These results indicate again that *mrc1a*$^+$*;*4C4$^+$ cells are distinct from other microglia subpopulations.

We further tested this relationship by lineage tracing *pu1*$^+$ cells from the yolk sac. To do this, we created *Tg(pu1:eos)* animals that express the photoconvertible protein Eos with *pu1* regulatory regions. Then, in *Tg(pu1:eos); Tg(mrc1a:egfp)* animals, we photoconverted single yolk sac *pu1*$^+$ cells at 24 hpf, grew the animals to 56 hpf, and fixed

and stained for GFP (Figure 7N, Extended Data Figure 6K). If a portion of *pu1*$^{+}$ cells from the yolk sac are *mrc1a*$^{+}$, we would expect *mrc1a*$^{+}$;pEos^{+} cells in the brain. We detected two populations of *mrc1*$^{+}$ cells in the brain, *mrc1*$^{+}$*;*pEos^{+} or *mrc1*$^{+}$;pEos^{-}. The *mrc1*$^{+}$*;*pEos^{+} population is consistent with a yolk sac origin (Figure 7O). However, *mrc1*$^{+}$*;*pEos^{-} or *mrc1*$^{+}$*;pEos*$^{-}$*;*4C4^{+} cells are consistent with a non-yolk sac origin (Figure 7P). We also detected a third population that was pEos^{+};*mrc1*$^{-}$, likely indicating the *pu1*$^{+}$ cells we detect in the brain (Figure 7P). The simplest explanation for these results is that *mrc1a*$^{+}$*;*4C4^{+} microglia are distinct from other subpopulations of microglia that express *pu1* and that originate from the 24 hpf yolk sac.

mrc1a^{+} microglia expand in response to CNS injury

The response and expansion of microglia after CNS injury is a hallmark of the cell-type[47]. We thus sought to compare the responses of *mrc1a*$^{+}$-lymphatic dependent and *pu1*$^{+}$ populations to pathophysiological conditions in development. To do this, we chemogenetically ablated radial glia using *Tg(gfap:nfsb-mCherry)* animals, which express a nitroreductase-tagged mCherry under the *gfap* promoter[48]. When bathed in the prodrug metronidazole (MTZ), nitroreductase metabolizes MTZ into cytotoxic products to induce radial glia death. Treatment with MTZ from 48 to 72 hpf induced rapid loss of radial glia, which was assessed by mCherry fluorescence in the hindbrain and spinal cord versus uninjured DMSO-treated animals (Figure 8A-8B, Extended Data Figure 7A). Death of radial glia was observed just 24 hours after treatment and continued until 120 hpf, 3 days post injury (dpi) (Extended Data Figure 7A).

To assess whether *mrc1a*$^{+}$ microglia expand in response to this injury, we conducted the injury paradigm in *Tg(mrc1a:egfp);Tg(gfap:nfsb-mCherry)* animals and immunolabeled microglia with 4C4. By 3 dpi, *mrc1a*$^{+}$;4C4^{+} microglia had expanded seven-fold relative to uninjured DMSO-treated animals ($p < 0.0001$) and comprised on average 88% of the responding 4C4^{+} microglia (Figure 8C-8D). *mrc1a*$^{-}$;4C4^{+} microglia also expanded relative to uninjured controls ($p = 0.029$), but only four-fold and comprised only an average of 12% of the responding microglia. We also observed a significant expansion of *mrc1a*$^{+}$ only cells in response to injury ($p < 0.0001$) (Figure 8C-8D). Thus, *mrc1a*$^{+}$ microglia exhibit significant microgliosis in response to damage to the CNS.

To next examine the possibility that *Mrc1*$^{+}$ microglia are present in mammals after injury, we again analyzed scRNA sequencing data, in which microglia from adult mice were isolated from a focal demyelinating lesion caused by LPC injection or from the same region in saline injected control mice[29]. In LPC-injected mice, *Mrc1*$^{+}$ cells significantly increased in number compared to saline injected mice (Figure 8E; $p = 0.0267$). Comparing canonical microglia marker expression in *Mrc1*$^{+}$ and *Mrc1*$^{-}$ cells revealed no significant differences in expression of those genes(Extended Data Figures 7B-7C). Although the increase in *Mrc1*$^{+}$ microglia in the scRNA sequencing data of mouse injury does not distinguish between the upregulation of *Mrc1* in previously *Mrc1*$^{-}$ microglia or the expansion of an existing *Mrc1*$^{+}$ microglia population, it does indicate that *Mrc1*$^{+}$ microglia are more present after injury to the mammalian brain.

mrc1a^{+} microglia are independently responsive to injury

Given both *mrc1a*$^{+}$ and *pu1*$^{+}$ microglia populations are present during development and injury, we next investigated whether *mrc1a*$^{+}$ and *pu1*$^{+}$ microglia injury responses are independent, by treating *Tg(mrc1a:egfp)*; *Tg(gfap:nfsb-mCherry)* or *Tg(pu1:Gal4;UAS:gfp)*; *Tg(gfap:nfsb-mCherry)* animals with the Csf1r inhibitor, GW2850, from 24 to 120 hpf, and MTZ from 48 to 72 hpf to induce injury (Figure 8F). Treatment with the inhibitor reduced *pu1*$^{+}$ cells but not *mrc1a*$^{+}$;4C4^{+} microglia or *mrc1a*$^{+}$ only cells (Figure 8F, 8G), again supporting the conclusion that *mrc1a* microglia are independent of the *pu1*$^{+}$ subpopulation.

To test this hypothesis with a second approach, we treated *Tg(mrc1a:egfp)*; *Tg(gfap:nfsb-mCherry)* animals with inhibitors of lymphangiogenesis from 48 to 120 hpf and MTZ from 48 to 72 hpf to create the injury (Figure 8H, 8I)[41]. All four inhibitors successfully inhibited the development of lymphatic vessels (Extended Data Figures 8A-8E). Inhibitor-treated animals also exhibited a reduction in the abundance of *mrc1a*$^{+}$;4C4^{+} (Figure 8E-8F), demonstrating the response of *mrc1a*$^{+}$ microglia to the injury is altered when animals are treated with drugs that reduce lymphatic vessels.

To ask if *pu1*$^{+}$ microglia also require lymphatics to respond to the injury, we repeated two of the lymphatic inhibitor treatments in *Tg(pu1:Gal4;UAS:gfp); Tg(gfap:nfsb-mCherry)* animals dosed with MTZ from 48 to 72 hpf and immunostained with 4C4. Treatment with leflunomide and flunarizine did not cause a change in the number of *pu1*$^{+}$ cells (p=0.7053, p=0.5165) or *pu1*$^{+}$;4C4^{+} microglia (p = 0.14, p = 0.2981), indicating *pu1*$^{+}$ microglia injury response is not disrupted when the animal is exposed to drugs that inhibit lymphatics

(Extended Data Figures 8F-8I). Together these data indicate that *mrc1a*$^{+}$ and *pu1*$^{+}$ microglia respond independently to injury and thereby further establish that these populations are distinct.

DISCUSSION:

Here we demonstrate that the zebrafish brain is seeded by a *mrc1a*$^{+}$ microglia population that is dependent on lymphatic vessels. We also show that induction of a pathophysiological state in embryonic animals results in expansion of *mrc1a*$^{+}$ microglia. This expansion in disease states is disrupted by perturbations that alter lymphatic vessels.

Beyond microglia, the brain is populated with brain lymphatic endothelial cells (BLECs), fluorescent granular perithelial cells (FGPs), brain-border and perivascular macrophages, and Mato cells[26,27]. Unlike these populations, the *mrc1a*$^{+}$ cells in the parenchyma display distinguishing features expected of microglia. They are located in the parenchyma, clear debris that is largely localized to the parenchyma, demonstrate heterotypic recognition with other microglia, and label with the microglia specific-antibody 4C4, as well as Lcp1 and *apoeb*. Distinct from FGPs, these *mrc1a*$^{+}$ cells in zebrafish express lower levels of *mrc1a:egfp,* are not labeled with Flt4, Prox1 or *lyve1b*, and are located in the parenchyma and are present in the spinal cord where lymphatic vessels and FGPs have yet to form and colonize[25]. Unlike macrophage populations, *mrc1a*$^{+}$ microglia display contact-dependent repulsion away from other microglia populations in zebrafish.

We know that precursors from extraembryonic yolk sac blood islands give rise to primitive macrophages which then colonize the brain and differentiate into mature microglia[16,35]. Other waves of hematopoiesis occurring outside of the yolk sac may also generate microglia progenitors in both mice and zebrafish[19,20,22]. Interestingly, the earliest microglia colonize the human CNS (at ~4-5 gestational weeks) prior to the establishment of active circulation[12,13,49]. Avian chimera studies have similarly described early colonization prior to brain vascularization[49]; however, lineage tracing demonstrates that yolk sac-derived microglia precursors require active circulation to colonize the brain in mice[16]. Our results may help bridge the gap between these disparate findings: the earliest colonizing microglia precursors may arise from or depend on lymphatic endothelium, while a later wave of yolk sac-derived progenitors colonizes the brain after circulation.

There are several indications that lymphatic endothelial vessels could be a site of cytogenesis. In the developing embryo, much of the nascent vasculature is hemogenic[50]. In mice, primitive hematopoiesis that produces myeloid cells can occur through a hemogenic endothelial intermediate located in vasculature[30,51]. Later waves of hematopoiesis generate blood cells from hemogenic endothelium in the wall of the dorsal aorta[52–54], and in zebrafish this region gives rise to an additional wave of microglia colonization in the adult animal[19,20]. Which vascular endothelium is hemogenic is unresolved but blood cells can be generated from vascular endothelium in the heart and cranium[51,55–57]. The possibility that lymphatic vessels are required for a subset of early microglia progenitors and that cells in the head could produce these *mrc1a*$^{+}$ microglia is

surprising but logical given the previously demonstrated ability of intraembryonic vascular endothelium to generate immune-like cells[27,56,57]. An alternative possibility is that lymphatic vessels serve as migration routes for early microglia precursors. Lastly, recently the bone marrow of the skull of mice, has been shown to be hematopoietic in order to produce macrophages that can respond to injury of the brain[58]. Our experiments do not distinguish between these possibilities.

Since the rediscovery of the brain lymphatic system, it has been implicated in disease states[59,60]. Because of its recent characterization, it is unlikely that its potential role in microglia seeding of the brain would have been investigated. The mature brain lymphatics are also thought to develop postnatally in mice and at later larval stages of zebrafish[61], after Mrc1^{+} progenitors colonize the zebrafish brain interfaces. Whether the mammalian brain has similar embryonic lymphatics surrounding the brain, like in zebrafish (Figure 5A,B), is unclear. The use of timelapse imaging in zebrafish was essential to visualize cells within the lymphatic vessels and departure through vessels, but does not exclude the possibility that *mrc1a*$^{+}$ microglia are at some point derived from yolk sac cells. Our data only supports the conclusion that the more direct source of *mrc1a*$^{+}$ microglia in zebrafish is likely the head. Nonetheless, these data place lymphatics at the epicenter of *mrc1a*$^{+}$ microglia colonization. The role and necessity of pioneer microglia and lymphatics are intriguing avenues for future studies.

ACKNOWLEDGEMENTS

We thank Brant Weinstein (NIH) for sending us the *Tg(mrc1a:egfp)* animals, Dirk Seiger for p5e-*pu1*, and Wilson Clements for *Tg(lck:gfp) and Tg(fli1:gfp)* animals. We thank Beth Stevens, Tim Hammond, Kelly Monk, Chris Bennett, and Siyuan Zhang for their helpful comments and reagent guidance. We also thank Brent Redford, Sam Connell and 3i for imaging related questions, Sara Cole in the NDiiF Optical Microscopy Core for help with light sheet imaging (OMC/NDIIF and the National Science Foundation-Major Research Instrumentation Program 1919832) and IMARIS analysis, and Deborah Bang, Karen Heed, and Brittany Gervais for zebrafish housing and upkeep. This work was supported by the University of Notre Dame, the Elizabeth and Michael Gallagher Family, Centers for Zebrafish Research and Stem Cells and Regenerative Medicine at the University of Notre Dame, the Indiana Spinal Cord and Brain Injury Research with the Indiana State Board of Health(CJS), the Alfred P. Sloan Foundation(CJS), and the NIH (DP2NS117177)(CJS). The funders had no role in study design, data collection and analysis, decision to publish or preparation of the manuscript.

AUTHOR CONTRIBUTIONS STATEMENT

LAG, MRO, CAH performed the analysis, experimentation, writing, and editing of the manuscript. DFD performed experimentation. MRO, LAG and CJS conceived the study. CJS wrote and edited the manuscript and supervised and funded the project.

COMPETING INTERESTS STATEMENT

The authors declare no competing interests.

FIGURES LEGENDS:

Figure 1. Microglia-like cells express *mrc1a.* (A) Confocal z-projection of *Tg(sox10:megfp)*, *Tg(neurod:gfp), Tg(lck:gfp), Tg(fli1a:gfp), Tg(pu1:gfp), and Tg(mrc1a:egfp)* animals stained with 4C4 at 5 dpf. (B) The percentage of 4C4$^+$ cells that co-express GFP. Quantifications represent all CNS regions of animals (n=59 animals). (C) Confocal z-projection of *Tg(mrc1a:egfp)* animals stained with 4C4 at 5 dpf labeling microglia-like cells in different CNS regions. (D) The average number of cells located within different CNS regions. Imaging window for the brain equals 0.0027 mm^3, hindbrain equals 0.0027 mm^3, and spinal cord equals 0.0108 mm^3 representing the CNS of each animal (n=6 animals). (E) Confocal z-plane images of *Tg(mrc1a:egfp);Tg(gfap:nfsb-mCherry)* animals hybridized with RNAscope probes *apoeb* and *lyve1b* at 5 dpf. White arrows: *mrc1a*$^+$ only microglia. Cyan arrows: *mrc1a*$^+$;*apoeb*$^+$ microglia. (F) The average number of *mrc1a*$^+$ parenchyma cells with co-labeled marked expression across various lymphatic, BLECs, vascular endothelial cells, and canonical cell markers (n=31 animals). (G) Confocal z-projection of *Tg(mrc1a:egfp)* animals stained with 4C4 at 7 dpf and 15 dpf. (H) The average number of *mrc1a*$^+$ only, 4C4$^+$ only, and *mrc1a*$^+$;4C4$^+$ microglia in the brain imaging window (n=8 animals). (I) The average number of *mrc1a*$^+$ only, 4C4$^+$ only, and *mrc1a*$^+$;4C4$^+$ microglia in the spinal cord imaging window (n=8 animals). Imaging window equals a 0.0027 mm^3 region of the brain (A-I). Scale bar equals 10μm (A,C,E, G). Error bars denote ± SEM (B, D, F, H-I).

Figure 2. *mrc1a*$^+$ microglia function like traditional microglia. (A) IMARIS 3D surface renderings of 5 dpf *Tg(mrc1a:egfp)* animals stained with antibodies or other transgenic

animals to label debris from synaptic, neuronal, oligodendrocyte, microglia, or astroglia populations. White boxes: magnified region of engulfed debris puncta (right column). (B) The percentage of types of labeled debris cleared by *mrc1a*$^{+}$ microglia (n=32 animals). (C) The percentage of the types of labeled debris cleared by *pu1*$^{+}$ microglia (n=53 animals). (D) The average speed of *pu1*$^{+}$ only, and *mrc1a*$^{+}$ only microglia from 4 dpf to 5 dpf (Ordinary one-way ANOVA / Tukey's multiple comparisons test: *pu1* vs. *mrc1a* p=0.9732, Mean diff.=0.0571, DF=42, q=0.3141, SE of diff.=0.2571)(n=32 cells; n=7 animals). (E) The total distance traveled by *pu1*$^{+}$ only, and *mrc1a*$^{+}$ only microglia from 4 dpf to 5 dpf (Ordinary one-way ANOVA / Tukey's multiple comparisons test: *pu1* vs. *mrc1a*$^{+}$ p=0.3616, Mean diff.=-118.3, DF=42, q=1.948, SE of diff.=85.88)(n=32 cells; n=7 animals). (F) Confocal z-projections of *Tg(mrc1a:egfp);Tg(pu1:gal4-uas:tagrfp)* animals showing homotypic interactions between *pu1*$^{+}$ and *mrc1a*$^{+}$ microglia populations from 4 dpf to 5 dpf. White arrowheads: *mrc1a*$^{+}$ microglia, blue arrowheads: *pu1*$^{+}$ microglia. (G) The migration path of individual *pu1*$^{+}$ microglia and *mrc1a*$^{+}$ microglia traveled pre and post contact (n=3 animals). (H) The average maximum distance *pu1*$^{+}$ only, *mrc1a*$^{+}$ only, and *pu1*$^{+}$*;mrc1a*$^{+}$ microglia traveled post-contact (Ordinary one-way ANOVA / Tukey's multiple comparisons test: *mrc1a-mrc1a* vs. *pu1-pu1* p=0.9949, Mean diff.=-2.328, DF=15, q=0.1362, SE of diff.=24.17; *mrc1a-mrc1a* vs. *mrc1a-pu1* p=0.9135, Mean diff.=9.824, DF=15, q= *pu1-pu1* vs. *mrc1a-pu1* p=0.8711, Mean diff. = 12.15, DF=15, q=0.711, SE of diff=24.17)(n=7 animals). Imaging window equals 0.0027 mm^3 (A-C), 0.0081 mm^3 (D-H). Scale bar equals 10μm (A), 100μm (F). Error bars denote ± SEM (D-E, H).

Figure 3. *Mrc1a*$^{+}$ cells colonize the brain early in development. (A) Confocal z-projection of *Tg(mrc1a:egfp);Tg(mpeg1:mCherry)* animals stained with GFAP at 36 hpf (middle-A'') IMARIS 3D surface rendering of vessels (green) and *mrc1a*$^{+}$ microglia (orange) combined with a 10µm confocal z-projection slice stained with GFAP to label the glial limitans. The combined 3D surface rendering and confocal image were rotated 45 in the negative (A') and positive (A'') orthogonal z-plane to confirm the presence of *mrc1a*$^{+}$ cells inside the glial limitans (A') and absence of *mrc1a*$^{+}$ cells outside the glial limitans (A''). (B) Confocal z-projection of *Tg(mrc1a:egfp);Tg(pu1:Gal4;UAS:rfp)* animals stained with GFAP at 36 hpf (middle-B'). The same 3D view (wCs) of Confocal z-projection of *Tg(mrc1a:egfp);Tg(mpeg1:mCherry)* animals stained with GFAP at 48 hpf (middle-C'). The same 3D view (wDs) of confocal projection of *Tg(mrc1a:egfp);Tg(pu1:Gal4;UAS:rfp)* animals stained with GFAP at 48 hpf (middle-D'). D' represent the same 3D view was shaded as cortical glial *mrc1a*$^{+}$ microglia-like cells within the GFAP^{+} limitans (A-D, -DA''). White arrow *mrc1a*$^{+}$ microglia-like cells (A-D). Dashed blue boxes: vessels cross of insets represented in (E). Graphical illustrations of the embryonic zebrafish brain (magenta) and vessels (green) at 36 hpf (A' and (C' and D' middle upper right *Tg(mrc1a:egfp)* vessels cross (E). Ma sections highlighted by the White dashed arrowheads cores. (F) The total number of marked cells inside the glial limitans at 36 hpf and 48 hpf in *Tg(mrc1a:egfp);Tg(pu1:Gal4;UAS:rfp)* or *Tg(mrc1a:egfp);Tg(mpeg:dsred)* animals (A-

F) (n=29 animals). Imaging window equals a 0.0027 mm^3 region of the brain. Scale bar equals 10μm (A-E). Error bars denote ± SEM (F).

Figure 4. Mrc1 is expressed in developmental microglia in the mammalian brain (A) Schematic depicting Hammond et al. (2019) and Kracht et al. (2020) isolations. (B) UMAP of subclustering of E14.5, P4/5, and P30 cells from Hammond et al, upper left, and log-normalized gene expression of *Mrc1* and canonical microglia. (C) (left) Heatmap of expression of BAM and microglia genes from Utz et al. (2020)[34] across microglia and macrophage clusters from Hammond et al. (right) Box plots of single-cell gene set enrichment scores for the BAM and microglia gene sets across clusters. Enrichment scores are reported as AUC (area under curve), calculated using *AUCell*. (D) (top) Heatmap of expression of BAM and microglia signature genes across *Mrc1*$^+$ and *Mrc1*$^-$ microglia and Cluster 2 BAMs. (bottom) Box plots of single-cell gene set enrichment scores for the BAM and microglia gene sets across the *Mrc1*$^+$ and *Mrc1*$^-$ microglia and Cluster 2 BAMs. (E) (left) Percentage of microglia per sample in *Mrc1*-enriched Cluster 10 versus sample age. Error bars denote ± SEM. P-values correspond to two-sided Tukey's multiple comparisons test (E14.5 vs. P4/5 vs. P30: p= 0.2071) following significant ANOVA (p < 0.0001). (*right*) Percentage of microglia per sample that are *Mrc1*$^+$ (E14.5: n = 8; P4/5: n = 14; P30: n = 4). P-values correspond to Tukey's multiple comparisons te P30: p = 0.1102; P4/5 vs. P30: p < 0.0001) following significant ANOVA (p < 0.0001). (F) UMAP plot of clustering of immune cells from Kracht et al, (upper left). (upper right and lower row) log-normalized gene expression of *MRC1* and canonical microglia markers

overlaid on UMAP plots. (G) (left) Heatmap of expression of BAM and microglia genes, human orthologs of the genes identified from Utz et al, across clusters. (right) Box plots of gene set enrichment scores for the BAM and microglia gene sets across clusters. (H) (top) Heatmap of expression of BAM and microglia genes across *MRC1*+ and *MRC1*- microglia and Cluster 9 BAMs. (bottom) Box plots of single-cell gene set enrichment scores for the BAM and microglia gene sets across the *MRC1*+ and *MRC1*- microglia and Cluster 9 BAMs. For box plots in (C-D, G-H), the transecting line indicates median. Notches indicate 95% confidence interval surrounding median. Box boundaries indicate interquartile range (25% to 75%). Whiskers indicate minima and maxima.

Figure 5. *mrc1a*$^+$ microglia are dependent on lymphangiogenesis. (A) Z-projection of images from light sheet microscopy (top row) and IMARIS surface renderings (bottom two rows) of the brain and surrounding *mrc1a*$^+$ vessels at 3 dpf in *Tg(mrc1a:egfp);Tg(gfap:nfsb-mCherry)* animals. Black arrowheads: pseudocolored cyan *mrc1a*$^+$ microglia inside the *gfap*$^+$ boundary. (B) IMARIS surface rendering (left) of the 3 dpf brain and surrounding *mrc1a*$^+$ vessels with a 2.3 µm cross sectional slice through the center (right). White arrowheads: *mrc1a*$^+$ vessels outside the *gfap*$^+$ boundary. Blue arrowheads: *mrc1a*$^+$ microglia inside the *gfap*$^+$ boundary. (C) Confocal z-projection (left) and IMARIS 3D surface rendering (middle) of dorsal lymphatic vessels outside the glial limitans. C' graphical illustration of vessels the em at 48 hpf. Grey box: dorsal lymphatic vessel location of confocal images depicted in (D). (C-C'''') dorsal and lateral cross section (c.s cores of vessel cross sections. (D) Confocal image (left) and surface rendering (right)

from a 24-hour timelapse movie starting at 34 hpf showing an *mrc1a*$^{+}$ cell (blue arrowheads) located within an *mrc1a*$^{+}$ lymphatic vessel at 39.17 hpf. Black dashed box: magnified view of *mrc1a*$^{+}$ cell inside the vessel (bottom). (E) Images (top), overlay of the cell's migration path (middle), 4-hour timelapse surface rendered movie starting at 34 hpf in *Tg(mrc1a:egfp)* animals showing an *mrc1a*$^{+}$ cell (blue and black arrowheads) exiting and interacting with a lymphatic vessel. (F) Confocal z-projection of DMSO- vs lymphatic inhibitor (A77-1726)-treated *Tg(mrc1a:egfp)* animals stained with 4C4. Blue arrowheads: *mrc1a*$^{+}$;4C4^{+} microglia. (G) The percentage of microglia per imaging window that are *mrc1a*$^{+}$ in DMSO- vs lymphatic inhibitor (A71-1726, cinnarizine, flunarizine, or leflunomide)-treated animals (one-way ANOVA/Dunnett's comparisons: DMSO vs. A77-1726 p=0.0014, Mean diff.=7.269, DF=69, q=3.825, SE of diff=1.994; DMSO vs. cinnarizine p=0.0003, Mean diff.=8.486, DF=69, q=4.255, SE of diff.=1.994; DMSO vs. flunarizine p=0.02378, Mean diff.=4.95, DF=69, q=1.947, SE of diff.=2.542, DMSO vs. leflunamide p=0.0028, Mean diff.=6.825, DF=69, q=3.616, SE of diff=1.687) (n=61 animals). Scale bar equals 10μm (B-E), 100μm (A). Error bars denote ± SEM (G).

Figure 6. *mrc1a*$^{+}$ microglia are dependent on lymphangiogenesis and lymphatics in the head. (A) *Tg(mrc1a:egfp)* at 5 dpf. Blue arrowheads: developed lymphatic vessels. Purple arrowheads: disrupted lymphatic vessels. (B-C) Total number of microglia in uninjected, Cas9 only, and *flt4* gRNA/Cas9-injected animals that are *mrc1a+;*4C4+ (B) (one-way ANOVA/Tukey's multiple comparisons: uninjected vs. Cas9 only Mean diff = -2.667, DF=119, q=2.986, SE of diff=1.263, uninjected vs. *flt4* gRNA/Cas9 p=0.0389, Mean diff=2.899, DF=119, q=3.5, SE of diff=1.171, Cas9 only vs. flt4

gRNA/Cas9 p<0.0001, Mean diff=5.566, DF=119, q=6.719, SE of diff=1.171)(n=122 animals) or *pu1+;mrc1a+*;4C4+ (C) (one-way ANOVA/Tukey's multiple uninjected vs. Cas9 only injected p=0.4784, Mean diff=1.006, DF=77, q=1.646, SE of diff=0.8648; uninjected vs. flt4 gRNA/Cas9 injected p=0.9893, Mean diff=-0.1033, DF=77, q=0.1975, SE of diff=0.7398; Cas9 only injected vs. flt4 gRNA/Cas9 injected p=0.3578, mean diff=-1.11, DF=77, q=1.948, SE of diff=0.8058)(n=80 animals). (D) Schematic illustrating Verteporfin treatment. (E) Verteporfin- or Verteporfin + 640nm-treated *Tg(mrc1a:egfp)* animals at 24 hpf. White arrowheads: microglia within the brain imaging window. (F) Average number of *mrc1a*$^{+}$ cells in the brain imaging window (t-test: Verteporfin vs. Verteporfin + 640nm p=0.0042, DF=10, two-tailed) (n=12). (G) Unactivated and activated DMSO- or Verteporfin-treated *Tg(mrc1a:egfp)* animals. White arrowheads: blebbing vessels. (H) Average number of blebbed vessel areas (t-test: DMSO vs. Verteporfin p=0.0420, Verteporfin vs. +6h Verteporfin p=0.0002, +6h DMSO + 640 nm vs. +6h Verteporfin + 640 nm p<0.0001, +6h Verteporfin vs. +6h Verteporfin + 640 nm p=0.0013, Verteporfin + 640 nm vs. +6h Verteporfin + 640 nm p<0.0001; all DF=20 and all two-tailed)(n=108). (I) Schematic outlining the injection, photoconversion of *bactin:eos,* and IHC staining in *Tg(mrc1a:egfp)* animals. (J) *bactin:eos*-injected animals photoconverted in various regions at 24 hpf and stained with GFP at 56 hpf. (K) Average number of *mrc1a*$^{+}$*;pEos*$^{+}$ cells converted in various regions (t-test: brain vs. RBI p=0.0081, RBI vs. yolksac p=0.2997, brain vs. yolksac p=0.0619; all two-tailed)(n=17). (L) Average number of *mrc1a*$^{+}$*;pEos*$^{+}$;anti-GFP^{+} cells (t-test: brain vs. RBI p=0.1664, RBI vs. yolksac p=0.5404, brain vs. yolksac p=0.0767; all two-tailed)(n=17). Imaging window equals

0.0027 mm^3 (E,G,J). Scale bars: 10μm (E), 50μm (A,G). Error bars denote ± SEM (B-C, F, H, K-L).

Figure 7. *mrc1a*$^+$;4C4$^+$ microglia are distinct from yolk sac-derived microglia. (A) 5 dpf *Tg(mrc1a:egfp);Tg(pu1:gal4-uas:tagrfp)* animals stained with 4C4. (B) Average number of cells in the CNS imaging window with varied expression. Imaging window represents 0.0027 mm^3 of the brain. Colored rectangles underneath graph labels correspond to expression patterns in (A)(n=9) (C) *Tg(mrc1a:egfp);Tg(pu1:Gal4;UAS:rfp)* animals 36 hpf-56 hpf. (D) Anatomical schematic of the imaging window in (C). (E) Average age various types of microglia colonize the brain (one-way ANOVA / Dunnet multiple comparisons: *mrc1a*$^+$ only vs. *pu1*$^+$ only p=0.0163, *pu1*$^+$ only vs. *mrc1a*$^+$;*pu1*$^+$ p=0.2844, *mrc1a*$^+$ only vs. *mrc1a*$^+$;*pu1*$^+$ p=0.2163). (F) Graphical illustration outlining our CRISPR/Cas9 *spi1b* single-gRNA injection experiment. (G-J) The total number of *pu1*$^+$ (G), *pu1*$^+$;*mrc1a*$^+$;4C4$^+$ (+++) (H), *mrc1a*$^+$ (I), and *mrc1a*$^+$;4C4$^+$ (J) cells in *spi1b* sgRNA injected animals compared to uninjected controls (t-test, *spi1b* sgRNA injected vs. uninjected: *pu1*$^+$ only p<0.0001, +++ p=0.0010, mrc1a$^+$ only p=0.0763, *mrc1a*$^+$;4C4$^+$ p=0.0967; all two-tailed)(n=41 G-J). (K) Average number of marked variants per imaging window across treatment groups (t-test, DMSO vs. GW2850: 4C4$^+$ only p=0.9132, *pu1*$^+$ only p=0.0015, *mrc1a*$^+$ only p=0.0533, 4C4$^+$;*mrc1a*$^+$ p=0.06598, 4C4$^+$;*mrc1a*$^+$;*pu1*$^+$ p>0.9999; all two-tailed)(n=8 animals). (L-M) Average number of microglia in uninjected and Cas9 only animals compared to *flt4* gRNA injected animals that were *pu1*$^+$ only (L) (one-way ANOVA / Tukey's multiple comparisons: uni Mean diff =0.3453, DF=77, q=1.536, SE of diff=0.3179; uninjected vs. *flt4* gRNA/Cas9

injected p=0.2527, Mean diff=0.2719, DF=77, q=2.26, SE of diff=0.2719; Cas9 injected vs. *flt4* gRNA/Cas9 injected p=0.9513, Mean diff=0.08919, DF=77, q=0.4259, SE of diff=0.2962) (n=80) or *pu1*$^{+}$*;mrc1a*$^{+}$ (M) (one-way ANOVA/Tukey's multipl
uninjected vs. Cas9 injected p=0.9625, Mean diff=0.08, DF=77, q=0.3727, SE of diff=0.3035; uninjected vs. *flt4* gRNA/Cas9 injected p=0.9533, Mean diff=0.08333, DF=77, q=0.4167, SE of diff=0.2828; Cas9 injected vs. *flt4* gRNA/Cas9 injected p=0.8046, Mean diff=0.1633, DF=77, q=0.8696, SE of diff=0.2596)(n=80). (N) Schematic illustrating the single-cell photoconversion and IHC in (O) and (P). (O) *Tg(mrc1a:egfp);Tg(pu1:eos)* animals at 56 hpf. (P) Average number of *pEos*$^{+}$ cells with marked expression at 56 hpf (n=12). Imaging window equals 0.0027 mm^3 of the brain (A-P). Scale bar equals 10μm (A, C, O). Error bars denote ± SEM (B, E, G-M, P).

Figure 8. *mrc1a*$^{+}$*;*4C4^{+} microglia expand in response to CNS injury. (A) Graphical illustration of MTZ drug treatment and staining. (B) Graphical illustration (left) and confocal z-projection (right) of the injury paradigm in 5 dpf animals. (C) Tiled confocal z-projection from a DMSO control and MTZ-treated 5 dpf *Tg(mrc1a:egfp);Tg(gfap:nfsb-mCherry)* zebrafish stained with 4C4 representing the entire animal. Individual *mrc1a*$^{+}$*;*4C4^{+} microglia (blue arrowheads) and a larger, expanded cluster (dashed blue box) can be seen. (D) Number of cells with marked expression in DMSO- vs MTZ-treated animals per imaging window (t-test, DMSO vs. MTZ: 4C4^{+} onlyp=0.0288, *mrc1a*$^{+}$ only p<0.0001, 4C4^{+};*mrc1a*$^{+}$ p<0.0001; all two tailed)(n=9). (E) Percentage of microglia that express at least one read of *Mrc1* from saline control- vs. LPC-injected P100 mice (data from Hammond et al., 2019) (t-test: saline vs. LPC p=0.0267; two tailed)(n=6). (F) The

average number of marked variants per imaging window in GW2580 + MTZ-treated vs. DMSO + MTZ-treated control animals(t-test, DMSO + MTZ vs. GW2850 + MTZ: *pu1*$^{+}$ only p=0.0215, *mrc1a*$^{+}$ only p=0.2077, 4C4^{+}*;pu1*$^{+}$ only p=0.1842, 4C4^{+}*;mrc1a*$^{+}$ only p=0.6479; all two-tailed)(n=24). (G) Representative confocal z-projection of *Tg(mrc1a:egfp);Tg(gfap:nfsb-mCherry)* and *Tg(pu1:gal4-uas:tagrfp);Tg(gfap:nfsb-mCherry)* animals stained with 4C4. (H) Representative confocal z-projections of 5 dpf *Tg(mrc1a:egfp);Tg:gfap:nfsb-mCherry)* animals stained with 4C4. Blue arrowheads: *mrc1a*$^{+}$*;*4C4^{+} microglia. Grey dashed line: glial limitans, microglia above dashed line (purple arrowheads) are inside the CNS and cells below the dashed line are *pu1*$^{+}$ macrophages. (I) The percentage of *mrc1a*$^{+}$ microglia in lymphatic inhibitor-treated animals compared to DMSO + MTZ control animals (one-way ANOVA/Dunnett's comparisons: DMSO + MTZ vs. A77-1726 + MTZ p=0.1301, Mean diff=17.59, DF=72, q=2.232, SE of diff=7.884; DMSO + MTZ vs. cinnarizine + MTZ p=0.0124, Mean diff=20.79, DF=72, q=3.13, SE of diff=6.644; DMSO + MTZ vs. flunarizine + MTZ p=0.9184, Mean diff=8.694, DF=72, q=0.8282, SE of diff=10.5; DMSO + MTZ vs. leflunomide + MTZ p=0.3860, MEan diff=13.19, DF=72, q=1.673, SE of diff=7.884)(n=75). Imaging windows: six 0.0027 mm^3 regions per animal, or 3000μm quantified to include the entire CNS of each animal (A-D, F), one 0.0027 mm^3 region per animal (F-I). Scale bars: 10μm (G, H) 100μm (B,C). Error bars denote ± SEM (D-F, I).

REFERENCES:

1. Miyamoto, A. *et al.* Microglia contact induces synapse formation in developing somatosensory cortex. *Nat. Commun.* **7**, (2016).

2. Schafer, D. *et al.* Microglia sculpt postnatal neuronal circuits in an activivty and complement-dependent manner. *Neuron* **74**, 691–705 (2012).
3. Paolicelli, R. C. *et al.* Synaptic pruning by microglia is necessary for normal brain development. *Science (80-.).* **333**, 1456–1458 (2011).
4. Cunningham, C. L., Martinez-Cerdeno, V. & Noctor, S. C. Microglia Regulate the Number of Neural Precursor Cells in the Developing Cerebral Cortex. *J. Neurosci.* **33**, 4216–4233 (2013).
5. Marín-Teva, J. L. *et al.* Microglia Promote the Death of Developing Purkinje Cells. *Neuron* **41**, 535–547 (2004).
6. Wakselman, S. *et al.* Developmental neuronal death in hippocampus requires the microglial CD11b integrin and DAP12 immunoreceptor. *J. Neurosci.* **28**, 8138–8143 (2008).
7. Ueno, M. *et al.* Layer v cortical neurons require microglial support for survival during postnatal development. *Nat. Neurosci.* **16**, 543–551 (2013).
8. Shigemoto-Mogami, Y., Hoshikawa, K., Goldman, J. E., Sekino, Y. & Sato, K. Microglia enhance neurogenesis and oligodendrogenesis in the early postnatal subventricular zone. *J. Neurosci.* **34**, 2231–2243 (2014).
9. Alexandria N. Hughes & Bruce Appel. Microglia phagocytose myelin sheaths to modify developmental myelination. *Nat. Neurosci.* (2020). doi:10.1016/j.expneurol.2008.09.010
10. Choi, B. H. Hematogenous cells in the central nervous system of developing human embryos and fetuses. *J. Comp. Neurol.* **196**, 683–694 (1981).
11. Andjelkovic, A. V., Nikolic, B., Pachter, J. S. & Zecevic, N.

Macrophages/microglial cells in human central nervous system during development: An immunohistochemical study. *Brain Res.* **814**, 13–25 (1998).

12. Monier, A. *et al.* Entry and distribution of microglial cells in human embryonic and fetal cerebral cortex. *J. Neuropathol. Exp. Neurol.* **66**, 372–382 (2007).
13. Verney, C., Monier, A., Fallet-Bianco, C. & Gressens, P. Early microglial colonization of the human forebrain and possible involvement in periventricular white-matter injury of preterm infants. *J. Anat.* **217**, 436–448 (2010).
14. Menassa, D. A. & Gomez-Nicola, D. Microglial dynamics during human brain development. *Front. Immunol.* **9**, (2018).
15. Monier, A., Evrard, P., Gressens, P. & Verney, C. Distribution and Differentiation of Microglia in the Human Encephalon during the First Two Trimesters of Gestation. *J. Comp. Neurol.* **499**, 565–582 (2006).
16. Ginhoux, F. *et al.* Fate Mapping Analysis Reveals That Adult Microglia Derive from Primitive Macrophages. *Science (80-.).* **330**, 841–845 (2010).
17. Herbom, P., Thisse, B. & Thisse, C. Zebrafish Early Macrophages Colonize Cephalic Mesenchym e and D eveloping Brain , Retina , and Epiderm is through a M-CSF Receptor-D ependent Invasive Process. *Dev. Biol.* **288**, 274–288 (2001).
18. Casano, A. M., Albert, M. & Peri, F. Developmental Apoptosis Mediates Entry and Positioning of Microglia in the Zebrafish Brain. *Cell Rep.* **16**, 897–906 (2016).
19. Xu, J. *et al.* Temporal-Spatial Resolution Fate Mapping Reveals Distinct Origins for Embryonic and Adult Microglia in Zebrafish. *Dev. Cell* **34**, 632–641 (2015).
20. Ferrero, G. *et al.* Embryonic Microglia Derive from Primitive Macrophages and Are Replaced by cmyb-Dependent Definitive Microglia in Zebrafish. *Cell Rep.* **24**,

130–141 (2018).

21. Chen, S. K. *et al.* Hematopoietic origin of pathological grooming in Hoxb8 mutant mice. *Cell* **141**, 775–785 (2010).
22. Chen, H. *et al.* Fate mapping via CCR2-CreER mice reveals monocyte-to-microglia transition in development and neonatal stroke. 1–14 (2020).
23. Ohnmacht, J. *et al.* Spinal motor neurons are regenerated after mechanical lesion and genetic ablation in larval zebrafish. *Development* **143**, 1464–1474 (2016).
24. Peri, F. & Nüsslein-Volhard, C. Live Imaging of Neuronal Degradation by Microglia Reveals a Role for v0-ATPase a1 in Phagosomal Fusion In Vivo. *Cell* **133**, 916–927 (2008).
25. Jung, H. M. *et al.* Development of the larval lymphatic system in zebrafish. *Development* **144**, 2070–2081 (2017).
26. van Lessen, M. *et al.* Intracellular uptake of macromolecules by brain lymphatic endothelial cells during zebrafish embryonic development. *Elife* **6**, 1–24 (2017).
27. Galanternik, M. V. *et al.* A novel perivascular cell population in the zebrafish brain. *Elife* **6**, 1–28 (2017).
28. Shin, M. *et al.* Vegfc acts through ERK to induce sprouting and differentiation of trunk lymphatic progenitors. *Dev.* **144**, 531 (2017).
29. Hammond, T. R. *et al.* Single-Cell RNA Sequencing of Microglia throughout the Mouse Lifespan and in the Injured Brain Reveals Complex Cell-State Changes. *Immunity* **50**, 253-271.e6 (2018).
30. Plein, A., Fantin, A., Denti, L., Pollard, J. W. & Ruhrberg, C. Erythro-myeloid progenitors contribute endothelial cells to blood vessels. *Nature* **562**, 223–228

(2018).

31. Koltowska, K. *et al.* Vegfc Regulates Bipotential Precursor Division and Prox1 Expression to Promote Lymphatic Identity in Zebrafish. *Cell Rep.* **13**, 1828–1841 (2015).

32. Green, L. A., Nebiolo, J. C. & Smith, C. J. Microglia exit the CNS in spinal root avulsion. *PLOS Biol.* **17**, e3000159 (2019).

33. Kracht, L. *et al.* Human fetal microglia acquire homeostatic immune-sensing properties early in development. *Science (80-.).* **369**, 530–537 (2020).

34. Utz, S. G. *et al.* Early Fate Defines Microglia and Non-parenchymal Brain Macrophage Development. *Cell* **181**, 557-573.e18 (2020).

35. Kierdorf, K. *et al.* Microglia emerge from erythromyeloid precursors via Pu . 1- and Irf8-dependent pathways. *Nat. Publ. Gr.* **16**, 273–280 (2013).

36. Bennett, M. L. *et al.* New tools for studying microglia in the mouse and human CNS. *Proc. Natl. Acad. Sci.* **113**, E1738–E1746 (2016).

37. Butovsky, O. *et al.* Identification of a unique TGF-β-dependent molecular and functional signature in microglia. *Nat. Neurosci.* **17**, 131–143 (2014).

38. Herbomel, P., Thisse, B. & Thisse, C. Ontogeny and behaviour of early macrophages in the zebrafish embryo. *Development* **126**, 3735–3745 (1999).

39. Goldmann, T. *et al.* Origin, fate and dynamics of macrophages at CNS interfaces HHS Public Access. *Nat Immunol* **17**, 797–805 (2016).

40. Smith, C. J., Morris, A. D., Welsh, T. G. & Kucenas, S. Contact-Mediated Inhibition Between Oligodendrocyte Progenitor Cells and Motor Exit Point Glia Establishes the Spinal Cord Transition Zone. *PLoS Biol.* **12**, e1001961 (2014).

41. Astin, J. W. *et al.* An in vivo antilymphatic screen in zebrafish identifies novel inhibitors of mammalian lymphangiogenesis and lymphatic-mediated metastasis. *Mol. Cancer Ther.* **13**, 2450–2462 (2014).

42. Zhang, L. *et al.* VEGFR-3 ligand-binding and kinase activity are required for lymphangiogenesis but not for angiogenesis. *Cell Res.* **20**, 1319–1331 (2010).

43. Tammela, T. *et al.* Photodynamic ablation of lymphatic vessels and intralymphatic cancer cells prevents metastasis. *Sci. Transl. Med.* **3**, (2011).

44. Kilarski, W. W. *et al.* Optimization and regeneration kinetics of lymphatic-specific photodynamic therapy in the mouse dermis. *Angiogenesis* **17**, 347–357 (2014).

45. Elmore, M. R. P. *et al.* Colony-stimulating factor 1 receptor signaling is necessary for microglia viability, unmasking a microglia progenitor cell in the adult brain. *Neuron* **82**, 380–397 (2014).

46. Erblich, B., Zhu, L., Etgen, A. M., Dobrenis, K. & Pollard, J. W. Absence of colony stimulation factor-1 receptor results in loss of microglia, disrupted brain development and olfactory deficits. *PLoS One* **6**, (2011).

47. Li, Q. & Barres, B. A. Microglia and macrophages in brain homeostasis and disease. *Nat. Rev. Immunol.* (2017). doi:10.1038/nri.2017.125

48. Smith, C. J., Johnson, K., Welsh, T. G., Barresi, M. J. F. & Kucenas, S. Radial glia inhibit peripheral glial infiltration into the spinal cord at motor exit point transition zones. *Glia* **64**, 1138–1153 (2016).

49. Cuadros, M. A., Martin, C., Coltey, P., Almendros, A. & Navascués, J. First appearance, distribution, and origin of macrophages in the early development of the avian central nervous system. *J. Comp. Neurol.* **330**, 113–129 (1993).

50. Gritz, E. & Hirschi, K. K. Specification and function of hemogenic endothelium during embryogenesis. *Cell. Mol. Life Sci.* **73**, 1547–1567 (2016).

51. Lancrin, C. *et al.* The haemangioblast generates haematopoietic cells through a haemogenic endothelium stage. *Nature* **457**, 892–895 (2009).

52. Swiers, G. *et al.* Early dynamic fate changes in haemogenic endothelium characterized at the single-cell level. *Nat. Commun.* **4**, (2013).

53. Boisset, J. C. *et al.* In vivo imaging of haematopoietic cells emerging from the mouse aortic endothelium. *Nature* **464**, 116–120 (2010).

54. Jaffredo, T., Gautier, R., Eichmann, A. & Dieterlen-Lièvre, F. Intra-aortic hemopoietic cells are derived from endothelial cells during ontogeny. *Development* **125**, 4575–4583 (1998).

55. Jordan, H. E. Evidence of hemogenic capacity of endothelium. *Anat. Rec.* **10**, 417–420 (1916).

56. Nakano, H. *et al.* Haemogenic endocardium contributes to transient definitive haematopoiesis. *Nat. Commun.* **4**, 1–10 (2013).

57. Li, Z. *et al.* Mouse embryonic head as a site for hematopoietic stem cell development. *Cell Stem Cell* **11**, 663–675 (2012).

58. A. Cugurra, T. Mamuladze, J. Rustenhoven, T. Dykstra, G. Beroshvili, Z. J. Greenberg, W. Baker, Z. Papadopoulos, A. Drieu, S. Blackburn, M. Kanamori, S. Brioschi, J. Herz, L. G. Schuettpelz, M. Colonna, I. Smirnov, J. K. Skull and vertebral bone marrow are myeloid reservoirs for the meninges and CNS parenchyma. *Science (80-.).* **in press**, 1–17 (2021).

59. Da Mesquita, S. *et al.* Functional aspects of meningeal lymphatics in ageing and

Alzheimer's disease. *Nature* **560**, 185–191 (2018).

60. Louveau, A. *et al.* Structural and functional features of central nervous system lymphatic vessels. *Nature* **523**, 337–341 (2015).

61. Castranova, D. *et al.* Live Imaging of Intracranial Lymphatics in the Zebrafish. *Circ. Res.* **128**, 42–58 (2021).

METHODS:

Data Availability

Data that supports the findings of this study are available in the Source Data tables. All data collected for the study are included in the figures. All code for the single-cell RNA sequencing data analysis in this manuscript can be accessed at https://github.com/michael-r-odea/Green_ODea_2022.

Experimental Model and Subject Details:

All animal studies were approved by the University of Notre Dame Institutional Animal Care and Use Committee. Zebrafish strains used for this study include: *Tg(mrc1a:egfp)*[25], *Tg(pu1:Gal4;UAS:tagrfp)*[62], *Tg(pu1:Gal4;UAS:gfp)*[62], *Tg(gfap:nfsb-mCherry)*[48], *Tg(sox10:mrfp)*[63], *Tg(sox10:megfp)*[64], *Tg(neurod:gfp)*[65], *Tg(neurod:rfp)*[66], *Tg(lck:gfp)*[67], *Tg(fli1a:gfp)*[68], *Tg(nbt:dsred)*[69], *Tg(pu1:eos) (*generated here*) and Tg(mpeg1:mCherry)*[69]. Pairwise matings produced embryos and embryos total darkness. Animals were staged by hours or days post fertilization (hpf and dpf)[70]. Stable germline transgenic lines were used. Embryos of either sex were used for all experiments.

Method Details

In vivo imaging

Animals were anesthetized with 3-amino-benzoic acid ester (Tricaine), enveloped in 0.8% low-melting point agarose and mounted accordingly for best imaging results. Animals were flat mounted on their right side, back mounted, or mounted dorsally in glass-

bottomed 35 mm Petri dishes[32,71]. Images were acquired on a spinning disk confocal microscope custom built by 3i technology© as previously described[71,72]. Images in timelapse microscopy were collected every 5 min for 18-48 hours depending on the experiment. Adobe Illustrator, IMARIS, and ImageJ were used to process images. Brightness and contrast were enhanced in presented images.

Light sheet microscopy

The 3 dpf embryonic brain, surrounding lymphatic vessels, and *mrc1a*$^{+}$ cells inside the *gfap*$^{+}$ labeled brain of *Tg(mrc1a:egfp);Tg(gfap:nfsb-mCherry)* animals were imaged using light sheet microscopy. Animals were anesthetized with Tricaine, enveloped in 1% low-melting point agarose, and mounted in a 100 µL glass capillary tube (Blaubrand, Germany). Light sheet microscopy was performed using a MuVi-SPIM system (Bruker) equipped with dual detection, 16x water-immersion objective lenses (N.A. 0.8, Nikon) and Orca Flash 4.0 V3 sCMOS cameras (Hamamatsu). Images were captured at 32X magnification using a 2x lens magnification changer. Image processing was performed using LuxControl software (version 3.4.0, Bruker). Further 3D surface reconstructions of the light sheet images of the *gfap*$^{+}$ brain and *mrc1a*$^{+}$ labeled vessels and cells inside *gfap*$^{+}$ brain were created using IMARIS.

Immunohistochemistry

The primary antibodies used in this study include 4C4 (1:50, mouse, Seiger, Becker and Becker Labs) (Ohnmacht et al., 2016)[23], GFP (1:500, chicken, Kerafast, EMU101), Lcp1

(1:500, rabbit, GeneTex, GTX134697), Prox1 (1:500, rabbit, AngioBio, 11-002), Flt4 (1:500, rabbit, Kerafast, ES1002), GFAP (1:500, rabbit, ZIRC, AB_1--13806), acetylated tubulin (1:250, mouse, Sigma-Aldrich catalog #T7451), Synapsin 1/2 (1:1000, rabbit, Synaptic Systems, catalog #106 102), SV2A (1:500, mouse, DHSB), and Znp-1 (1:500, mouse, DHSB). The secondary antibodies used in this study include Alexa Fluor 405, goat anti-rabbit (1:600, ThermoFisher, catalog #: A-11034), Alexa Fluor 647, goat anti-rabbit (1:600, ThermoFisher, catalog #: R3121), Alexa Fluor 647 goat anti-chicken (1:600, ThermoFisher, catalog #: A21449), and Alexa Fluor 647, goat anti-mouse (1:600, ThermoFisher, catalog #: A-21235). Staining was performed using the protocol in Nichols & Smith (2019)[72]. Larvae were fixed at 36 hpf, 48 hpf, 72 hpf, 4 dpf, 5 dpf, 6 dpf, 7 dpf and 15 dpf in fresh 4% PFA in 0.1% PBS Triton-X.

RNAscope *in situ* hybridization

The probes used were: *apoeb* (1:50, 80 µL, C3, ACD) and *lyve1b* (1:50, 80 µL, C2, ACD). RNAScope was performed using the protocol detailed in Kikel-Coury et al., (2020,2021)[73,74]. Larvae were fixed at 5 dpf in 4% PFA at 25°C for 30 minutes.

Single-cell RNA sequencing analysis

Data Sources

Single-cell RNA-sequencing data from Hammond et al. (2019)[29] and Kracht et al. (2020)[33] was obtained from the NCBI GEO under the access numbers GSE121654 and GSE141862, respectively.

Hammond et al. (2019) Analysis

Raw UMI count data was obtained from the NCBI GEO database for E14.5, P4, P5, and P30 samples. Analysis was performed using R (v4.1) and Seurat (v4.0.4)[75,76]. Cells expressing fewer than 400 or greater than 3,000 genes, cells with greater than 10,000 transcripts, and cells with greater than 3% of their transcripts mapping to the mitochondrial genome were excluded from further analysis to eliminate shallow reads, multiplets, and apoptotic cells, respectively. Expression data was log-normalized (UMIs per cell were divided by total UMIs per cell, natural-log transformed, and multiplied by a scale factor of 10,000) and integrated using Harmony[77]. Dimensionality reduction was performed via UMAP using 40 Harmony-corrected principal components, and hierarchical clustering was performed using HGC[78]. After removing 11 singlets, and cutting the resulting dendrogram at k = 11, we identified 11 clusters (7 microglia, 1 monocyte/macrophage, 1 endothelial, and 2 neuronal). We then selected the 7 microglia clusters and the monocyte/macrophage cluster for sub-clustering to identify microglial and macrophage subpopulations. We again batch corrected using Harmony and performed dimensionality reduction using UMAP (using 50 principal components), and performed sub-clustering on the resultant 69,862 cells using HGC. After removing 67 singlets which did not cluster, we cut the cluster dendrogram at k = 21 and merged terminal sibling branches when one sibling cluster included less than 600 cells to avoid focusing analysis on very rare cell subtypes. This yielded 16 clusters. One cluster, cluster 3, was identified as neurons on the basis of expression of canonical markers such as *Meg3*, and *Neurod6*. The remaining clusters expressed typical macrophage lineage markers. To identify these clusters as either microglia or border-associated macrophages (BAMs) in an unbiased

manner, we first identified embryonic microglia and BAM gene signatures from bulk RNA-sequencing data from Utz et al. (2020)[34]. FASTQ files were obtained from the NCBI GEO database (GSE146928), trimmed with TrimGalore (v0.6.6)[79], and mapped with Salmon (v1.5.2)[80]. DESeq2[81] was used to identify genes differentially expressed between microglia and BAMs across all embryonic ages. A log2-fold change threshold of ±1 and a multiple comparisons-adjusted p-value threshold of 0.05 were used to determine statistical significance. Significant differentially expressed genes were sorted by the baseMean expression to identify the genes most likely to be detected via scRNA-seq. The top 50 significant microglia markers and top 50 BAM markers by baseMean expression detected in the Hammond et al. (2019)[29] single-cell data were used to form the microglia and BAM gene signature sets. Genes in the microglia gene set were excluded if less than 20% of cells expressed the gene, to eliminate genes poorly detected in the dataset. Z-scored average log-normalized expression of genes in these sets across the macrophage-lineage clusters was visualized via heatmaps using the *ComplexHeatmap* package[82], and differential expression testing was performed using Seurat. Per-cell gene set enrichment scores for the microglia and BAM sets were calculated using *AUCell*[83] using default parameters. Clusters 1, and 4-16 were identified as microglia given their higher expression of the microglia gene set and lower expression of the BAM gene set. Cluster 2 was highly enriched in BAM genes and was classified as BAMs. Differential expression testing was performed using Seurat via Wilcoxon rank-sum test, and significance thresholds were set at ± 0.5 log2-fold change and $p < 0.01$. Microglia (from clusters 1, and 4-16) were further subsetted into *Mrc1*+ (log-normalized expression > 0) and *Mrc1*- (log-normalized expression = 0) groups and compared to the cluster 2

BAMs with the same previously used microglia and BAM gene sets. P100 LPC-injected and saline-injected control mouse raw UMI data was also obtained from the NCBI GEO database. Counts were log-normalized, and the proportion of *Mrc1*+ (log-normalized expression > 0) cells per sample was calculated. Cells from LPC-injected mice were then divided into *Mrc1*+ (log-normalized expression > 0) and *Mrc1*- groups and differential expression testing was performed using Seurat and a list of canonical microglia genes.

Kracht et al., (2020) Analysis

UMI count data was obtained from the NCBI GEO database, and analysis was performed using R (v4.1) and Seurat (v4.0.4)[75,76]. ENSEMBL gene IDs were converted to gene symbols using the EnsDB.Hsapiens.v79[84] Bioconductor package. Cells with fewer than 200 or greater than 3000 genes detected, greater than 90,000 reads per cell, or greater than 10% of reads mapping to the mitochondrial genome were removed from downstream analysis. The count data was log-normalized and integrated across sub-samples (separately sequenced runs from each sample) using Harmony[77]. Dimensionality reduction was performed via UMAP using 15 Harmony-corrected principal components, and hierarchical clustering was performed using HGC[78]. The clustering dendrogram was cut at k = 7, resulting in four microglia clusters, one neuronal cluster, one erythrocytic cluster, and one macrophage/monocyte cluster, classified by examining cluster-specific differentially expressed genes. The microglia and macrophage clusters were selected for subclustering, reintegrated using Harmony, and dimensionality reduction was again performed via UMAP using 10 corrected principal components followed by hierarchical clustering using HGC. The dendrogram was cut at k = 10, yielding one leukocyte cluster

and nine macrophage-lineage clusters. Murine microglia and BAM gene sets were identified from Utz et al. (2020)[34], and converted to human orthologs using the biomaRt package[85]. The top 50 microglia and top 50 BAM genes that were detectable in the Kracht et al. data were retained for gene sets. Gene set expression and enrichment analysis was performed as described above. Clusters 1-7 & 10 were identified as microglia on the basis of higher microglia gene set expression and lower expression of the BAM gene set, while cluster 9 was identified as BAMs and was highly enriched in BAM genes. Microglia (from clusters 1-7 & 10) were divided into *Mrc1*+ (log-normalized expression > 0) and *Mrc1*- (log-normalized expression = 0) partitions and DE testing was again performed using Seurat and the microglia and BAM gene sets as described above.

All data plots were generated using the Seurat, ggplot2, ggpubr, or ComplexHeatmap packages in R[76,82,86,87].

Chemical Treatments

Lymphatic inhibitor treatments

The chemical reagents used in these experiments were A77-1726 (Millpore Sigma Cat. 100128) at 2μM, cinnarizine (Alfa Aesar Cat. J64568) at 28uM, leflunomide (Alfa Aesar Cat. J65917) at 4μM, and flunarizine (Alfa Aesar Cat. J62969) at 5μM[41]. Stock solutions of each drug were stored at -20 with concentrations of 1% DMSO for A77-1726 and cinnarizine. For drugs with additional vehicles, stock solutions were stored at -20 with concentrations of 20% 2-hydroxypropyl-B-cyclodextrin for flunarizine and 1.5% carboxymethylcellulose (Alfa Aesar Cat A181105) for leflunomide. All treated embryos

were dechorionated at 24 hpf and then dosed each day from 24 hpf to 120 hpf. Control animals were also incubated with 1% DMSO in egg water (A77-1726, cinnarizine), 20% 2-hydroxypropyl-B-cyclodextrin in egg water (flunarizine), and 1.5% carboxymethylcellulose in egg water (leflunomide) daily from 24 hpf to 120 hpf. All drug values were selected and all lymphatic treatments were performed following a previous anti-lymphatic drug screen protocol[41.] Treated and control animals were then fixed and stained with 4C4 at 5 dpf following the protocol in Nichols & Smith (2019)[88].

Verteporfin (MedChemExpress, HY-B0146/CS-1950) was reconstituted in 100% DMSO and 10mM stock solutions were stored at -20C. All treated embryos were incubated with 1μM Verteporfin (0.0001% DMSO) from 0-24 hpf and PTU from 24-96 hpf. Verteporfin+640nm animals were dechorionated at 24 hpf, exposed to 640nm light (laser power 2, 100 ms exposure) in a 30μm stack at a step size of 1μm in the forebrain, midbrain, and regions just outside the brain, and then grown until 96 hpf. Exposure to 640nm light was achieved by dorsally mounting dechorionated, Verteporfin-treated animals and angling the animals' tails upward animals were flush with the bottom of the glass dish and therefore exposed to the laser. Positioning for the 30μm stack was achieved by setting a midpoint 15μm into the animal from the most dorsal view of the intracranial lymphatic vessels surrounding the midbrain.

Csf1r *inhibitor treatments*

The chemical reagent used in this experiment is GW2580 (ApexBio). Stock solutions of 10μM were stored at -20C with concentrations of 1% in DMSO[32]. All embryos were

dechorionated at 24 hpf and incubated with 3 mL egg water until desired treatment time. Animals were treated daily starting at 24 hpf until 144 hpf. Control animals were incubated daily with 1% DMSO in egg water from 24 hpf to 144 hpf.

Generation of transgenics and plasmids

bactin:eos

Gateway cloning was used to generate *bactin:eos*. The p5e-*bactin*[89], pMe-*eos*[90], 3pe-pA[89] and 395 destination vectors were recombined with LR clonase to produce pCS-DFD14 *(bactin:eos)*[89]. In one cell *Tg(mrc1a:gfp)* animals, 1 nl of inject mix composed of 25 ng/ul of *bactin:eos* and 75 ng/ul of RNA transposase. F_0 animals were used for all *bactin:eos* experiments.

Tg(pu1:eos)

Gateway cloning was used to generate *pu1:eos*. The p5e-*pu1*[62], pMe-*eos*[90], p3e-pA[89] and 395 destination vectors were recombined with LR clonase to produce *pu1:eos*[89]. One cell AB animals were then injected with 1 nl of injection mix composed of 12.5 ng/ul of *pu1:eos* and 75 ng/ul of RNA transposase[89]. F_0 animals were screened as Eos^+ and then grown to adulthood. F_0 animals were crossed to AB and Eos+ progeny were identified then grown to adulthood as the F_1 population. All *Tg(pu1:eos)* experiments were completed on stable transgenic animals that were outcrossed for at least 2 generations.

Photoconversion Experiments

bactin:eos region photoconversions

Tg(mrc1a:egfp) embryos were injected with a *bactin:eos* construct at the one-cell stage. Embryos were then grown to 24 hpf. Confocal z-stack images of the green v488 and red v561 channels were to confirm positive *Eos* expression pre-conversion and confirm negative expression in the red channel prior to photoconversion. *bactin:eos* cells were then photoconverted using 5 ms bursts of v405 nm laser exposure to specified regions on our confocal microscope using mVector. Photoconversions were performed in three groups with one distinct region of the animal converted; the yolk sac, the RBI, and the brain vessels. The brain vessel converted animals involved photoconverting the *bactin:eos* cells lining the vessels of the brain using the line tool in Slidebook software. Single *bactin:eos* cells were photoconverted in the RBI and yolk sac regions using the cursor tool in Slidebook software. The RBI region represents the early rostral blood islands located in between the developing head and yolk sac. The *bactin:eos* cells located along the outside of the yolk sac represent the yolk sac region. Following photoconversion, we took post-photoconversion images in the green v488 and red v561 channels to confirm successful conversion of the photoconverted *Eos* protein from green v488 to red v561. Animals were then grown to 56 hpf, fixed, and stained with GFP (v647) and GFAP (v405) following the immunohistochemistry protocol in Nichols & Smith (2019). Confocal z-stack images were taken of Eos^{+} cells in the laterally mounted right side of the brain 0.0027 mm^3 imaging window in stained 56 hpf animals.

<u>*Tg(pu1:eos)* single-cell photoconversions</u>

We created *Tg(pu1:eos)* animals and crossed them to *Tg(mrc1a:egfp)* animals. *Tg(pu1:eos);Tg(mrc1a:egfp)* embryos were grown to 24 hpf. Pre-conversion confocal z-

stack images were taken in the green v488 and red v561 channels to confirm there was no non-specific photoconversion. Single *pu1*$^{+}$ cells were then photoconverted using a 5 ms v405 nm laser pulse in the embryonic yolk sac at 24 hpf following the single-cell photoconversion protocol in Green and Smith, 2018[91]. Following photoconversion, post-conversion confocal z-stack images were taken in the green v488 and red v561 channels to confirm expression of the converted Eos^{+} protein. Photoconverted animals were then grown to 56 hpf and then fixed and stained with 4C4 and GFP following the immunohistochemistry protocol in Nichols & Smith (2019)[72,88]. Confocal z-stack images were taken of photoconverted Eos^{+} cells in the laterally mounted right side of the brain 0.0027 mm^{3} imaging window in stained 56 hpf animals. We scored the different expression profiles of *mrc1a*$^{+}$*,*p-Eos^{+}*,* and 4C4^{+} cells.

Genetic Perturbation

flt4 genetic perturbation

Two synthetic gRNA duplexes, crRNA;trRNA[92], (crRNA - altR system, IDT) were created (5'-GCGTTAGCGTTAATCACAAGC-3') and (5'-AAACGCTTAACGCGAGTCATTGGCC-3') that targeted the translated region of *flt4* at exon 2 and 3*. Tg(mrc1a:egfp) and Tg(mrc1a:egfp);Tg(pu1:Gal4;UAS:rfp)* embryos were injected with a sgRNA at the one-cell stage and imaged at 5 dpf. The sequences of primers for genotyping of *Tg(mrc1a:egfp)* only animals injected with *flt4* gRNAs were: 5'-TAGGTCTGGTGAATGGGTTTTC-3' (forward, exon-2) AAAAGCTCTGTGCTGTGACAAA-3' (reverse, exon-2) CTGGCCTGAAGAGTCTTTGAGT-3' (forward, exon-3)

CACAGCTCTTACCTCGAACAAA-3' (reverse). Following genomic DNA amplification, PCR products were purified and a T7 endonuclease I digestion (New England Biolabs, Cat# M0302L) to detect mutation was performed. F_0 mutants were confirmed by the presence of two bands, an uncut (288bp) and cut (<200bp) band. Wildtype animals were identified by a single uncut (288bp) band. Uninjected and Cas9 only injected *Tg(mrc1a:egfp)* animals served as controls. Animals were genotyped after scoring to ensure blinded quantification.

spi1b genetic perturbation

A synthetic gRNA duplex, crRNA;trRNA[92], (crRNA - IDT) was created that targeted the translated region of *spi1b*. TGCATCCGTACAGAATGGAGGGG-3') that targeted the translated region of *spi1b*. *Tg(mrc1a:egfp); Tg(pu1:Gal4;UAS:rfp)* embryos were injected with a sgRNA at the one-cell stage and imaged at 5 dpf. The sequences of primers for genotyping of *spi1b* were: ACAGTTTTGAAAGCCCTT-TforwardA) and (5'CAAACGCAAAATAATGCAAAC (3' reverse). Following genomic DNA amplification, PCR products were purified and a T7 endonuclease I digestion (New England Biolabs, Cat# M0302L) to detect mutation was performed. F_0 mutants were confirmed by the presence of two bands, an uncut (288bp) and cut (<200bp) band. Wildtype animals were identified by a single uncut (288bp) band. Mutants in F_0 larvae were confirmed by Sanger sequencing of amplified genomic DNA. Uninjected *Tg(mrc1a:egfp)* animals served as a control. Animals were genotyped after scoring to ensure blinded quantification.

MTZ Ablation

To perform *gfap*-specific cell ablations, *Tg(gfap:nfsb-mCherry)* animals tagged with nitroreductase under a *gfap* promoter were used[48,93]. A 20mM Metronidazole (MTZ, Fisher Scientific, Cat# AC210340050) stock solution was made and protected from light. All embryos were dechorionated at 24 hpf and incubated with 3 mL egg water until desired treatment time[48]. Animals were dosed with 10mM MTZ in 0.0003% PTU and 1% DMSO in egg water and then incubated starting at 48 hpf. MTZ was removed at 72 hpf and replaced with 0.0003% PTU and 1% DMSO in egg water until desired imaging time. Control animals were incubated with 0.0003% PTU and 1% DMSO in egg water starting at 24 hpf until desired imaging time.

Quantification and statistical analysis

3i Slidebook software (Denver, CO) was used to generate composite z-images of microglia. All individual z-images were sequentially observed. IMARIS (Notre Dame Imaging Core) was used to create 3D surface renderings of microglia. All graphical data represent both the mean and individual values used in each experiment unless otherwise noted. All quantifications were performed using various plugins available in ImageJ (Bethesda, MD) and Microsoft Excel (Seattle, WA). GraphPad Prism (San Diego, CA) software was used to perform all statistical analysis. Full list of sample sizes, central tendency and variance, statistical tests, and p-values can be found in the Source Data tables.

No statistical methods were used to pre-determine sample sizes but our sample sizes are similar to those reported in previous publications[9,32,63,64]. All statistical tests were run with

biological replicates, not technical replicates. Healthy animals were randomly selected for experiments. No data points were excluded from analysis. Data distribution was assumed to be normal, but this was not formally tested. It is indicated where data collection and analysis performed were blinded. If not indicated, data collection and analysis were not performed blind to the conditions of the experiments. Each experiment was repeated at least twice with similar results.

Quantification of debris puncta

To visualize debris puncta, confocal images were taken of several *Tg(mrc1a:egfp)* and *Tg(pu1:Gal4;UAS:gfp)* animals stained with 4C4 and with other debris types labeled in magenta. 3D surface renderings were created of individual *mrc1a*$^{+}$ microglia using IMARIS (Notre Dame Imaging Core). To confirm the presence of debris within or outside an *mrc1a*$^{+}$ microglia, rotated the images up to 270 degrees in the orthogonal z-plane were used. Magenta puncta present inside green *mrc1a*$^{+}$ microglia were considered a type of debris cleared by the microglia population. If magenta puncta were not present inside green *mrc1a*$^{+}$ they were considered a type of debris not cleared by the microglia population.

Quantification of cell migration

To create the migration plots and calculate the distance *mrc1a*$^{+}$ and *pu1*$^{+}$ cells travel post-heterotypic or homotypic contact with another *mrc1a*$^{+}$ or *pu1*$^{+}$ cell, we timelapse imaged *Tg(mrc1a:egfp);Tg(pu1:Gal4;UAS:rfp)* animals from 36-56 hpf, 48-72hpf, and 72-96 hpf. We used the MTrackJ plugin in ImageJ to track the individual paths that *mrc1a*$^{+}$ only, *pu1*$^{+}$

only and *mrc1a*$^{+}$*;pu1*$^{+}$ cells traveled prior to contacting another marked cell throughout a 24-hour imaging window. We set the MTrackJ X,Y coordinates of the point of contact between the two cells as the origin for the migration plot. We also used the MTrackJ plugin in ImageJ to track the individual paths that *mrc1a*$^{+}$ only, *pu1*$^{+}$ only and *mrc1a*$^{+}$*;pu1*$^{+}$ cells traveled post-contact with another marked cell. The distance equation in Excel was used to measure the distance between the X, Y coordinates of the maximum distance each cell traveled post-contact and the X, Y coordinates of the origin (point of contact).

Quantification of lymphatic vessels

Lymphatic vessel number, length, and number of secondary sprouting event quantifications were represented following the quantitative methods listed in Astin et al. (2014)[41]. We used the freehand tracing tool in ImageJ to trace and measure the raw length of each lateral lymphatic vessel present in the brain of each DMSO control and lymphatic inhibitor treated animal. All further quantifications were performed using Excel and all statistical analyses were performed using GraphPad Prism.

Quantification of GFAP fluorescence

The mean gray value of *mCherry* fluorescence in the brain and spinal cord was measured by tracing the brain and spinal cord boundaries using the freehand selection tool in ImageJ. Then, the mean gray value of the background of each individual z-stack image was measured by drawing a small circle (or multiple small circles and averaging between them) in the upper right corner with the freehand selection tool. This data for each image was normalized by subtracting the background mean gray value from the mean gray

value inside the brain or spinal cord boundary. When treating with both lymphatic inhibitors and MTZ, fluorescence was normalized to the DMSO control group.

Supplemental Data

All supplemental data are provided in Source Data files for each main and Extended Data figure that contain all raw n-values, data values, and statistical data exported from GraphPad Prism (version 8). These data also contain results for normality tests. For all datasets that did not pass normality tests, secondary unpaired nonparametric t-test analysis were used and yielded similar p-values.

REFERENCES FOR METHODS

62. Sieger D, Moritz C, Ziegenhals T, Prykhozhij S, Peri F. Long-Range Ca2+ Waves Transmit Brain-Damage Signals to Microglia. Dev Cell. 2012;22: 1138–1148. doi:10.1016/j.devcel.2012.04.012

63. Kucenas S, Wang W-D, Knapik EW, Appel B. A Selective Glial Barrier at Motor Axon Exit Points Prevents Oligodendrocyte Migration from the Spinal Cord. J Neurosci. 2009;29: 15187–15194. doi:10.1523/JNEUROSCI.4193-09.2009

64. Kirby BB, Takada N, Latimer AJ, Shin J, Carney TJ, Kelsh RN, et al. In vivo time-lapse imaging shows dynamic oligodendrocyte progenitor behavior during zebrafish development. Nat Neurosci. 2006;9: 1506–1511. doi:10.1038/nn1803

65. Andermann P, Ungos J, Raible DW. Neurogenin1 defines zebrafish cranial sensory ganglia precursors. Dev Biol. 2002;251: 45–58. doi:10.1006/dbio.2002.0820

66. McGraw HF, Snelson CD, Prendergast A, Suli A, Raible DW. Postembryonic

neuronal addition in Zebrafish dorsal root ganglia is regulated by Notch signaling. Neural Dev. 2012;7: 23. doi:10.1186/1749-8104-7-23

67. Langenau DM, Ferrando AA, Traver D, Kutok JL, Hezel JPD, Kanki JP, et al. In vivo tracking of T cell development, ablation, and engraftment in transgenic zebrafish. Proc Natl Acad Sci U S A. 2004;101: 7369–7374. doi:10.1073/pnas.0402248101

68. Lawson ND, Weinstein BM. In vivo imaging of embryonic vascular development using transgenic zebrafish. Dev Biol. 2002;248: 307–318. doi:10.1006/dbio.2002.0711

69. Rosenberg AF, Wolman MA, Franzini-Armstrong C, Granato M. In Vivo Nerve-Macrophage Interactions Following Peripheral Nerve Injury. J Neurosci. 2012;32: 3898–3909. doi:10.1523/JNEUROSCI.5225-11.2012

70. Schilling TF. Stages of embryonic development of the zebrafish. Dev Dyn. 1995;203: 253–310. doi:10.1002/aja.1002030302

71. Nichols EL, Green LA, Smith CJ. Ensheathing cells utilize dynamic tiling of neuronal somas in development and injury as early as neuronal differentiation. Neural Dev. Neural Development; 2018;13: 19. doi:10.1186/s13064-018-0115-8

72. Nichols EL, Smith CJ. Pioneer axons employ
spinal cord. Nat Commun. Springer US; 2019;10: 562. doi:10.1038/s41467-019-08421-9

73. Kikel-Coury NL, Brandt JP, Correia IA, O'Dea M
Identification of astroglia-like cardiac nexus glia that are critical regulators of cardiac development and function. PLoS Biol. 2021;

74. Kikel-Coury NL, Green LA, Nichols EL, Zellmer AM, Pai S, Hedlund SA, et al. Pioneer Axons Utilize a Dcc Signaling-Mediated Invasion Brake to Precisely Complete Their Pathfinding Odyssey. J Neurosci. 2021;41: 6617 –6636. doi:10.1523/JNEUROSCI.0212-21.2021

75. R Core Team. R: A language and environment for statistical computing. R Foundation for Statistical Computing. In: Vienna, Austria [Internet]. 2021. Available: https://www.r-project.org/

76. Hao Y, Hao S, Andersen-Nissen E, Mauck WM, Zheng S, Butler A, et al. Integrated analysis of multimodal single-cell data. Cell. Cell; 2021;184: 3573-3587.e29. doi:10.1016/J.CELL.2021.04.048

77. Korsunsky I, Millard N, Fan J, Slowikowski K, Zhang F, Wei K, et al. Fast, sensitive and accurate integration of single-cell data with Harmony. Nat Methods. Springer US; 2019;16: 1289 –1296. doi:10.1038/s41592-019-0619-0

78. Zou Z, Hua K, Zhang X. HGC: fast hierarchical clustering for large-scale single-cell data. Bioinformatics. Oxford Academic; 2021;37: 3964 –3965. doi:10.1093/BIOINFORMATICS/BTAB420

79. Krueger F, James F, Ewels P, Afyounian E, Schuster-Boeckler B. FelixKrueger/TrimGalore: v0.6.7 - DOI via Zenodo. 2021; doi:10.5281/ZENODO.5127899

80. Patro R. Salmon provides fast and bias-aware quantification of transcript expression. 2017; doi:10.1038/nmeth.4197

81. Love MI, Huber W, Anders S. Moderated estimation of fold change and dispersion for RNA-seq data with DESeq2. Genome Biol. BioMed Central Ltd.; 2014;15: 1 –

21. doi:10.1186/S13059-014-0550-8/FIGURES/9

82. Gu Z, Eils R, Schlesner M. Complex heatmaps reveal patterns and correlations in multidimensional genomic data. doi:10.1093/bioinformatics/btw313

83. Aibar S, González-Blas CB, Moerman T, Huynh-Thu VA, Imrichova H, Hulselmans G, et al. SCENIC: Single-cell regulatory network inference and clustering. Nat Methods. 2017;14: 1083–1086. doi:10.1038/nmeth.4463

84. Bioconductor - EnsDb.Hsapiens.v79 [Internet]. [cited 29 Apr 2022]. Available: https://bioconductor.org/packages/release/data/annotation/html/EnsDb.Hsapiens.v79.html

85. Durinck S, Spellman PT, Birney E, Huber W. Mapping identifiers for the integration of genomic datasets with the R/Bioconductor package biomaRt. 2009; doi:10.1038/nprot.2009.97

86. Wickham H. ggplot2. Cham: Springer International Publishing; 2016; doi:10.1007/978-3-319-24277-4

87. Kassambara A. ggpubr: "ggplot2" based publ Available: https://rdrr.io/cran/ggpubr/

88. Nichols EL, Smith CJ. Synaptic-like Vesicles Facilitate Pioneer Axon Invasion. Curr Biol. Elsevier Ltd.; 2019; 1–13. doi:10.1016/j.cub.2019.06.078

89. Kwan KM, Fujimoto E, Grabher C, Mangum BD, Hardy ME, Campbell DS, et al. The Tol2kit: A multisite gateway-based construction Kit for Tol2 transposon transgenesis constructs. Dev Dyn. 2007;236: 3088–3099. doi:10.1002/dvdy.21343

90. Prendergast A, Linbo TH, Swarts T, Ungos JM, McGraw HF, Krispin S, et al. The

metalloproteinase inhibitor Reck is essential for zebrafish DRG development. Development. 2012;139: 1141–1152. doi:10.1242/dev.072439

91. Green L, Smith CJ. Single-cell Photoconversion in Living Intact Zebrafish. J Vis Exp. 2018; e57024–e57024. doi:10.3791/57024

92. Hoshijima K, Jurynec MJ, Klatt Shaw D, Jacobi AM, Behlke MA, Grunwald DJ. Highly Efficient CRISPR-Cas9-Based Methods for Generating Deletion Mutations and F0 Embryos that Lack Gene Function in Zebrafish. Dev Cell. Elsevier Inc.; 2019;51: 645-657.e4. doi:10.1016/j.devcel.2019.10.004

93. Johnson K, Barragan J, Bashiruddin S, Smith CJ, Tyrrell C, Parsons MJ, et al. Gfap-positive radial glial cells are an essential progenitor population for later-born neurons and glia in the zebrafish spinal cord. Glia. 2016;64: 1170–1189. doi:10.1002/glia.22990

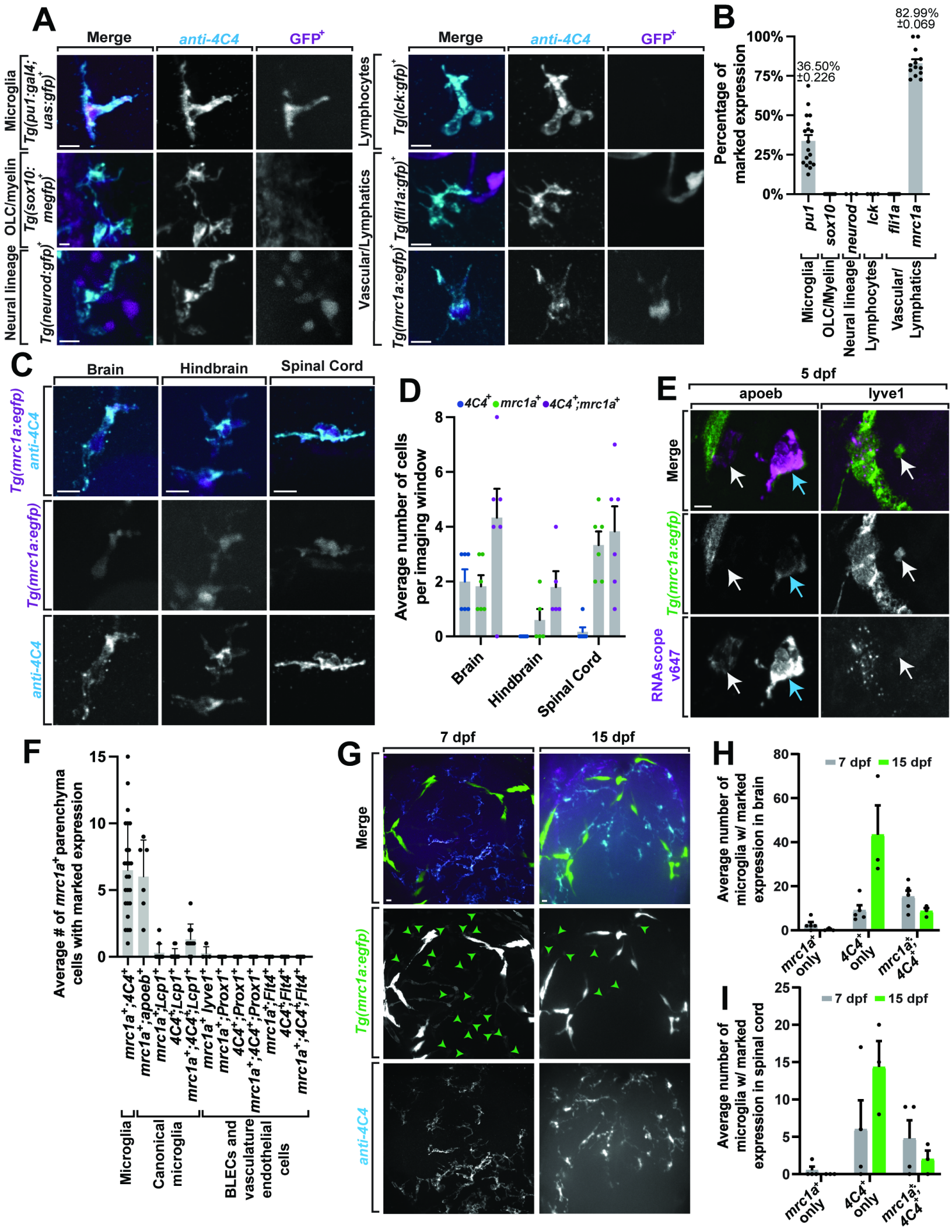
A
Merge
anti-4C4
GFP+
Microglia
Tg(pu1:gal4;uas:gfp)+
OLC/myelin
Tg(sox10:megfp)+
Neural lineage
Tg(neurod:gfp)+
Lymphocytes
Tg(lck:gfp)+
Vascular/Lymphatics
Tg(fli1a:gfp)+
Tg(mrc1a:egfp)+
B
Percentage of marked expression
100%
75%
50%
25%
0%
36.50% ±0.226
82.99% ±0.069
pu1
sox10
neurod
lck
fli1a
mrc1a
Microglia
OLC/Myelin
Neural lineage
Lymphocytes
Vascular/ Lymphatics
C
Brain
Hindbrain
Spinal Cord
Tg(mrc1a:egfp) anti-4C4
Tg(mrc1a:egfp)
anti-4C4
D
4C4+ mrc1a+ 4C4+;mrc1a+
Average number of cells per imaging window
8
6
4
2
0
Brain
Hindbrain
Spinal Cord
E
5 dpf
apoeb
lyve1
Merge
Tg(mrc1a:egfp)
RNAscope v647
F
Average # of mrc1a+ parenchyma cells with marked expression
15
10
5
0
mrc1a+;4C4+
mrc1a+;apoeb+
mrc1a+;Lcp1+
4C4+;Lcp1+
mrc1a+;4C4+;Lcp1+
mrc1a+;lyve1+
mrc1a+;Prox1+
4C4+;Prox1+
mrc1a+;4C4+;Prox1+
mrc1a+;Flt4+
4C4+;Flt4+
mrc1a+;4C4+;Flt4+
Microglia
Canonical microglia
BLECs and vasculature endothelial cells
G
7 dpf
15 dpf
Merge
Tg(mrc1a:egfp)
anti-4C4
H
Average number of microglia w/ marked expression in brain
80
60
40
20
0
7 dpf
15 dpf
mrc1a+ only
4C4+ only
mrc1a+; 4C4+
I
Average number of microglia w/ marked expression in spinal cord
25
20
15
10
5
0
7 dpf
15 dpf
mrc1a+ only
4C4+ only
mrc1a+; 4C4+

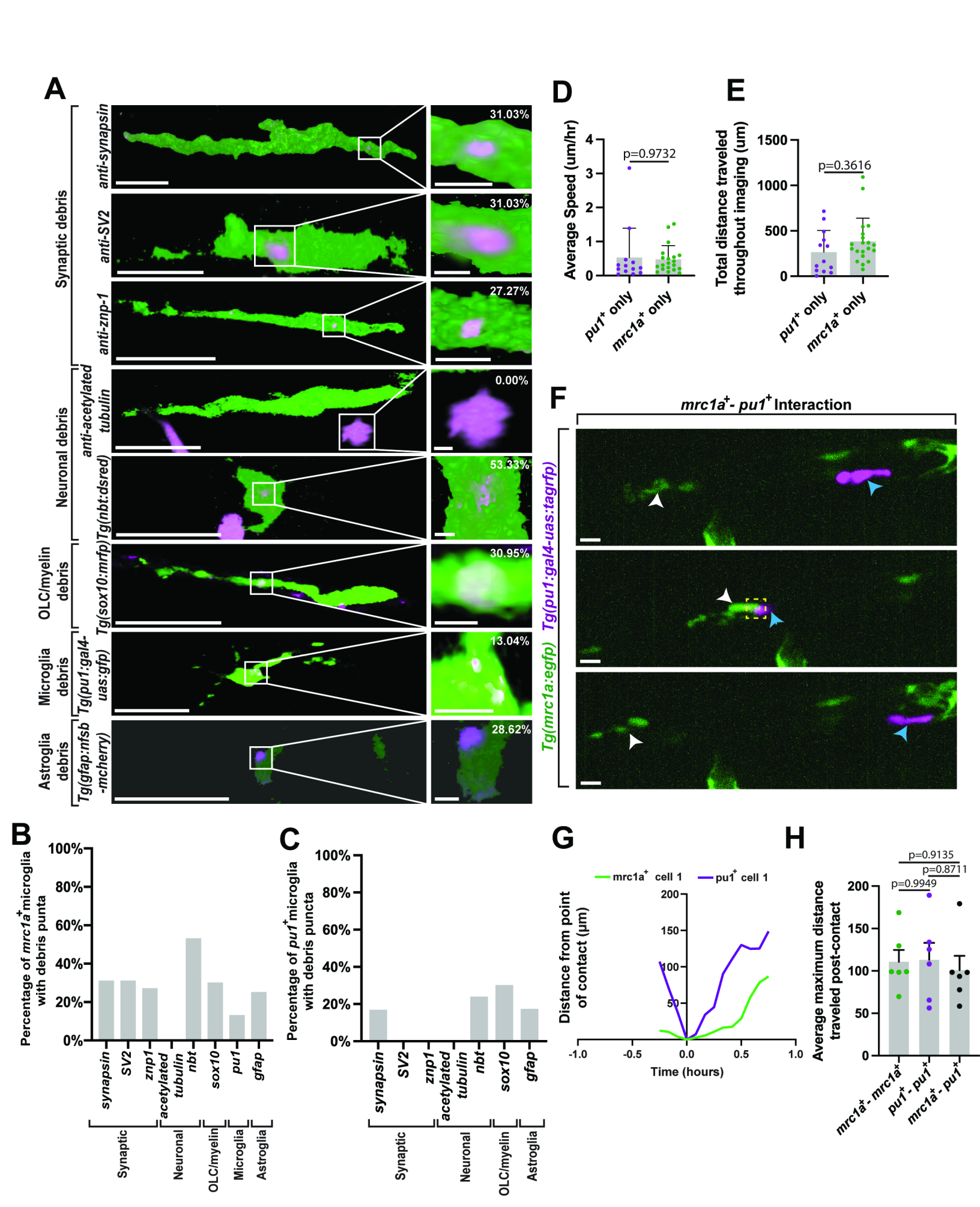
A
Synaptic debris
anti-synapsin
anti-SV2
anti-znp-1
Neuronal debris
anti-acetylated tubulin
Tg(nbt:dsred)
OLC/myelin debris
Tg(sox10:mrfp)
Microglia debris
Tg(pu1:gal4-uas:gfp)
Astroglia debris
Tg(gfap:nfsb-mcherry)
31.03%
31.03%
27.27%
0.00%
53.33%
30.95%
13.04%
28.62%
D
Average Speed (um/hr)
p=0.9732
pu1+ only
mrc1a+ only
E
Total distance traveled throughout imaging (um)
p=0.3616
pu1+ only
mrc1a+ only
F
mrc1a+- pu1+ Interaction
Tg(mrc1a:egfp)
Tg(pu1:gal4-uas:tagrfp)
B
Percentage of mrc1a+ microglia with debris punta
synapsin
SV2
znp1
acetylated tubulin
nbt
sox10
pu1
gfap
Synaptic
Neuronal
OLC/myelin
Microglia
Astroglia
C
Percentage of pu1+ microglia with debris puncta
G
mrc1a+ cell 1
pu1+ cell 1
Distance from point of contact (µm)
Time (hours)
H
Average maximum distance traveled post-contact
p=0.9135
p=0.8711
p=0.9949
mrc1a+- mrc1a+
pu1+- pu1+
mrc1a+- pu1+

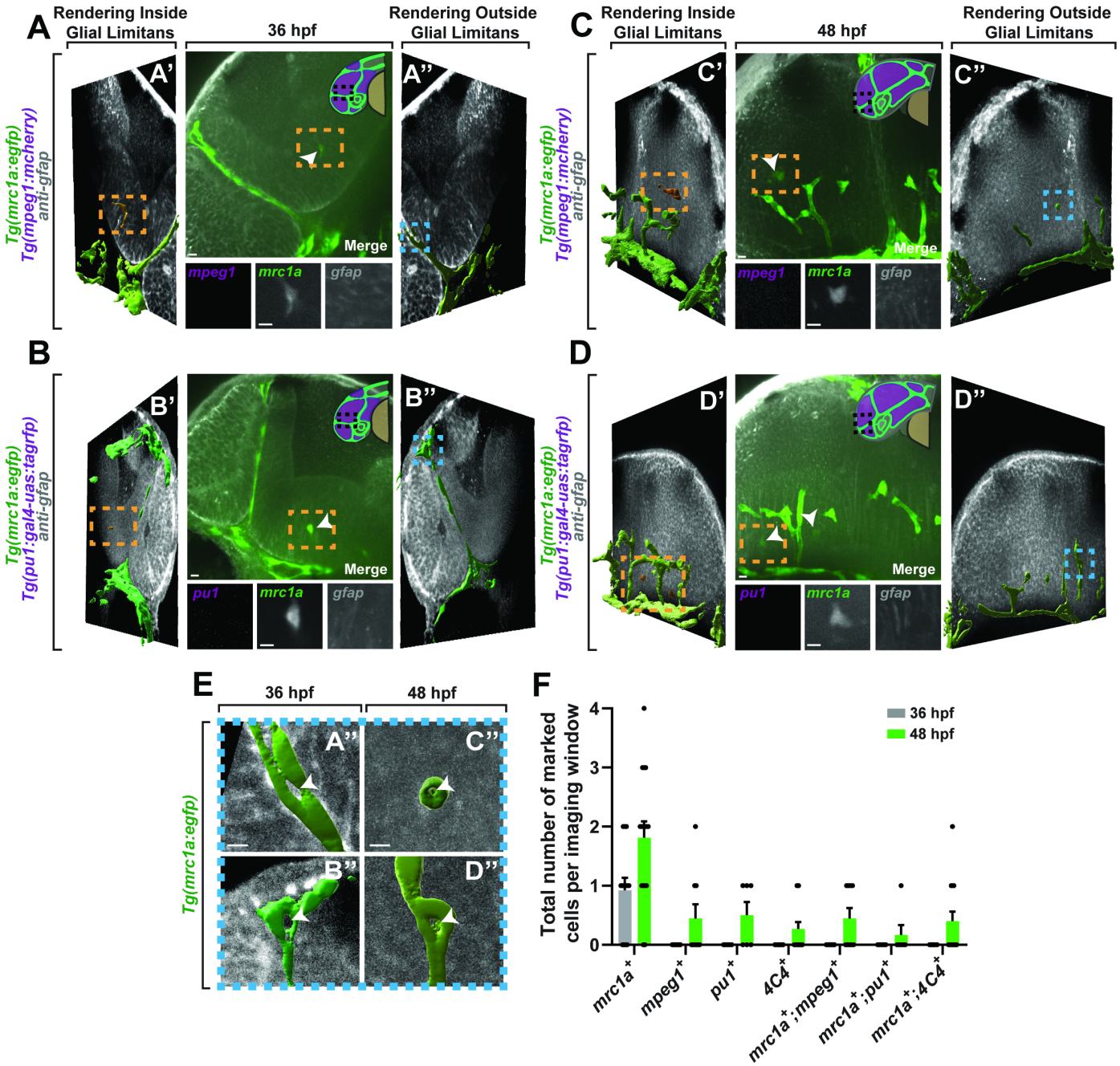
A
Rendering Inside Glial Limitans
36 hpf
Rendering Outside Glial Limitans
C
Rendering Inside Glial Limitans
48 hpf
Rendering Outside Glial Limitans
Tg(mrc1a:egfp)
Tg(mpeg1:mcherry)
anti-gfap
A'
A''
C'
C''
Merge
mpeg1
mrc1a
gfap
B
D
Tg(mrc1a:egfp)
Tg(pu1:gal4-uas:tagrfp)
anti-gfap
B'
B''
D'
D''
Merge
pu1
mrc1a
gfap
E
36 hpf
48 hpf
Tg(mrc1a:egfp)
A''
C''
B''
D''
F
Total number of marked cells per imaging window
36 hpf
48 hpf
0
1
2
3
4
mrc1a+
mpeg1+
pu1+
4C4+
mrc1a+;mpeg1+
mrc1a+;pu1+
mrc1a+;4C4+

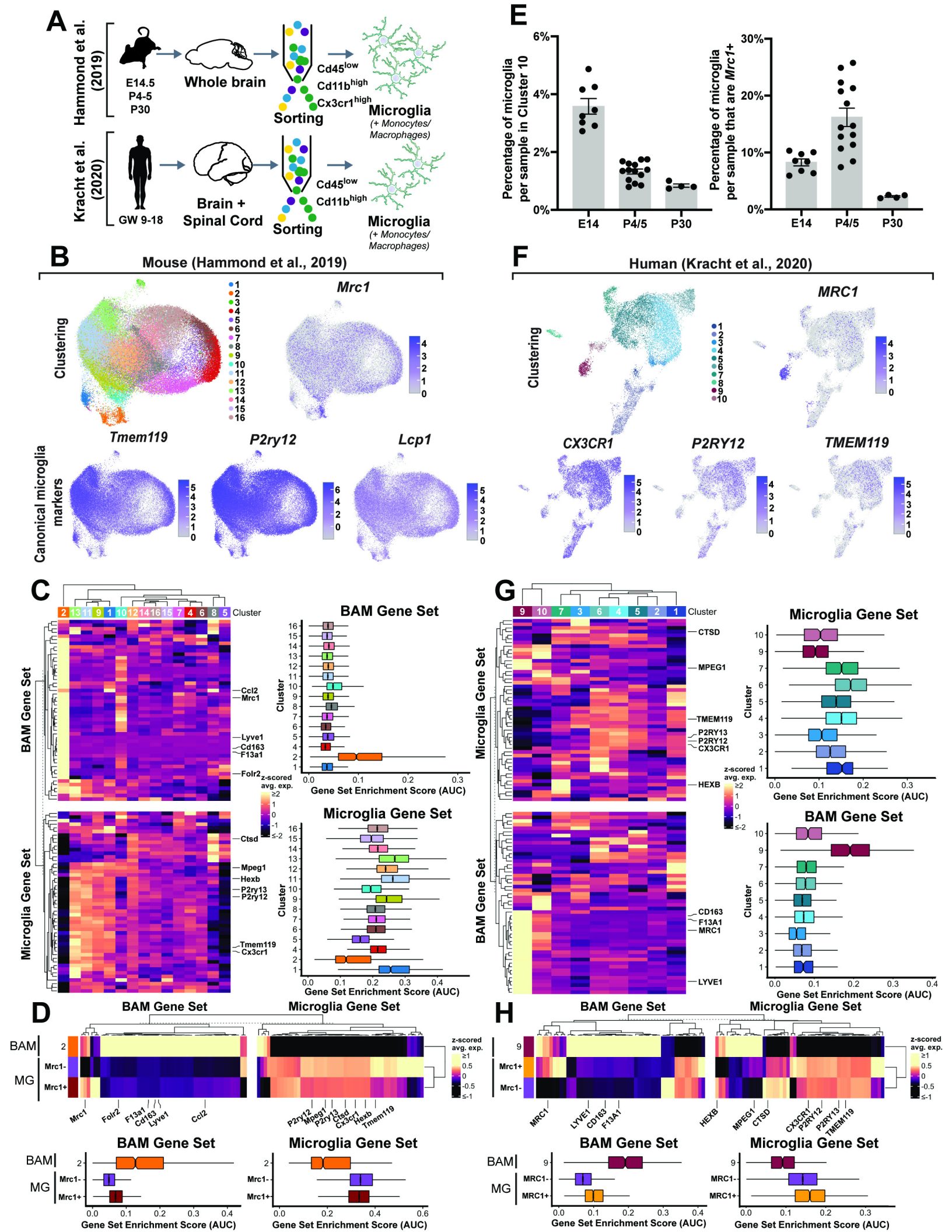
A
Hammond et al. (2019)
E14.5
P4-5
P30
Whole brain
Cd45low
Cd11bhigh
Cx3cr1high
Sorting
Microglia
(+ Monocytes/ Macrophages)
Kracht et al. (2020)
GW 9-18
Brain + Spinal Cord
Cd45low
Cd11bhigh
Sorting
Microglia
(+ Monocytes/ Macrophages)
E
Percentage of microglia per sample in Cluster 10
6%
4%
2%
0%
E14
P4/5
P30
Percentage of microglia per sample that are Mrc1+
30%
20%
10%
0%
E14
P4/5
P30
B
Mouse (Hammond et al., 2019)
Clustering
Mrc1
Canonical microglia markers
Tmem119
P2ry12
Lcp1
F
Human (Kracht et al., 2020)
Clustering
MRC1
CX3CR1
P2RY12
TMEM119
C
Cluster
BAM Gene Set
Ccl2
Mrc1
Lyve1
Cd163
F13a1
Folr2
Microglia Gene Set
Ctsd
Mpeg1
Hexb
P2ry13
P2ry12
Tmem119
Cx3cr1
z-scored avg. exp.
Gene Set Enrichment Score (AUC)
G
Cluster
Microglia Gene Set
CTSD
MPEG1
TMEM119
P2RY13
P2RY12
CX3CR1
HEXB
BAM Gene Set
CD163
F13A1
MRC1
LYVE1
z-scored avg. exp.
Gene Set Enrichment Score (AUC)
D
BAM Gene Set
Microglia Gene Set
BAM
MG
Mrc1-
Mrc1+
Mrc1
Folr2
F13a1
Cd163
Lyve1
Ccl2
P2ry12
Mpeg1
P2ry13
Ctsd
Cx3cr1
Hexb
Tmem119
z-scored avg. exp.
Gene Set Enrichment Score (AUC)
H
BAM Gene Set
Microglia Gene Set
MRC1
LYVE1
CD163
F13A1
HEXB
MPEG1
CTSD
CX3CR1
P2RY12
P2RY13
TMEM119
z-scored avg. exp.
Gene Set Enrichment Score (AUC)

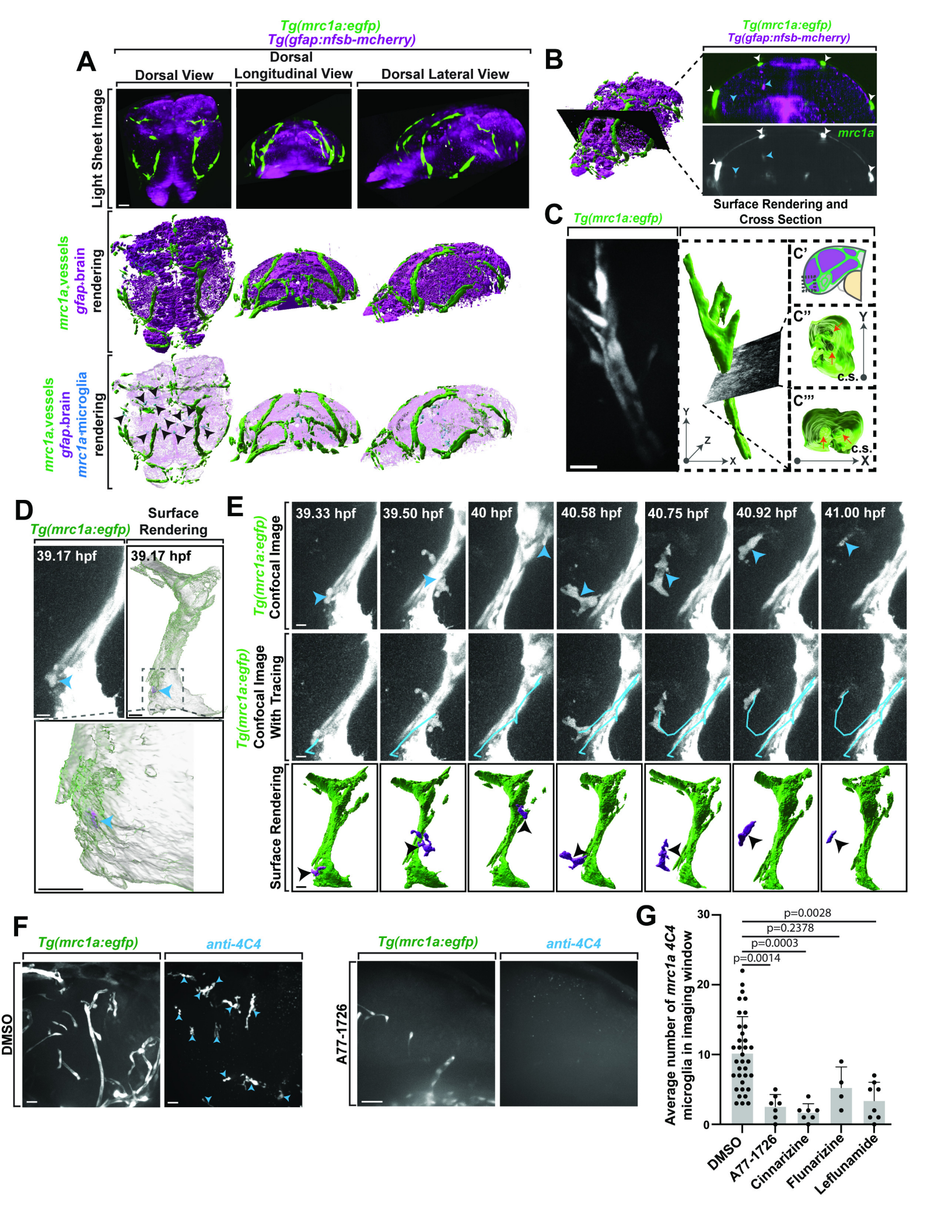
A
Tg(mrc1a:egfp)
Tg(gfap:nfsb-mcherry)
Dorsal
Dorsal View
Dorsal Longitudinal View
Dorsal Lateral View
Light Sheet Image
mrc1a+vessels gfap+brain rendering
mrc1a+vessels gfap+brain mrc1a+microglia rendering
B
Tg(mrc1a:egfp)
Tg(gfap:nfsb-mcherry)
mrc1a
C
Tg(mrc1a:egfp)
Surface Rendering and Cross Section
C'
C''
C'''
c.s.
Y
Z
X
D
Tg(mrc1a:egfp)
Surface Rendering
39.17 hpf
39.17 hpf
E
Tg(mrc1a:egfp) Confocal Image
Tg(mrc1a:egfp) Confocal Image With Tracing
Surface Rendering
39.33 hpf
39.50 hpf
40 hpf
40.58 hpf
40.75 hpf
40.92 hpf
41.00 hpf
F
Tg(mrc1a:egfp)
anti-4C4
DMSO
A77-1726
G
Average number of mrc1a 4C4 microglia in imaging window
p=0.0028
p=0.2378
p=0.0003
p=0.0014
30
20
10
0
DMSO
A77-1726
Cinnarizine
Flunarizine
Leflunamide

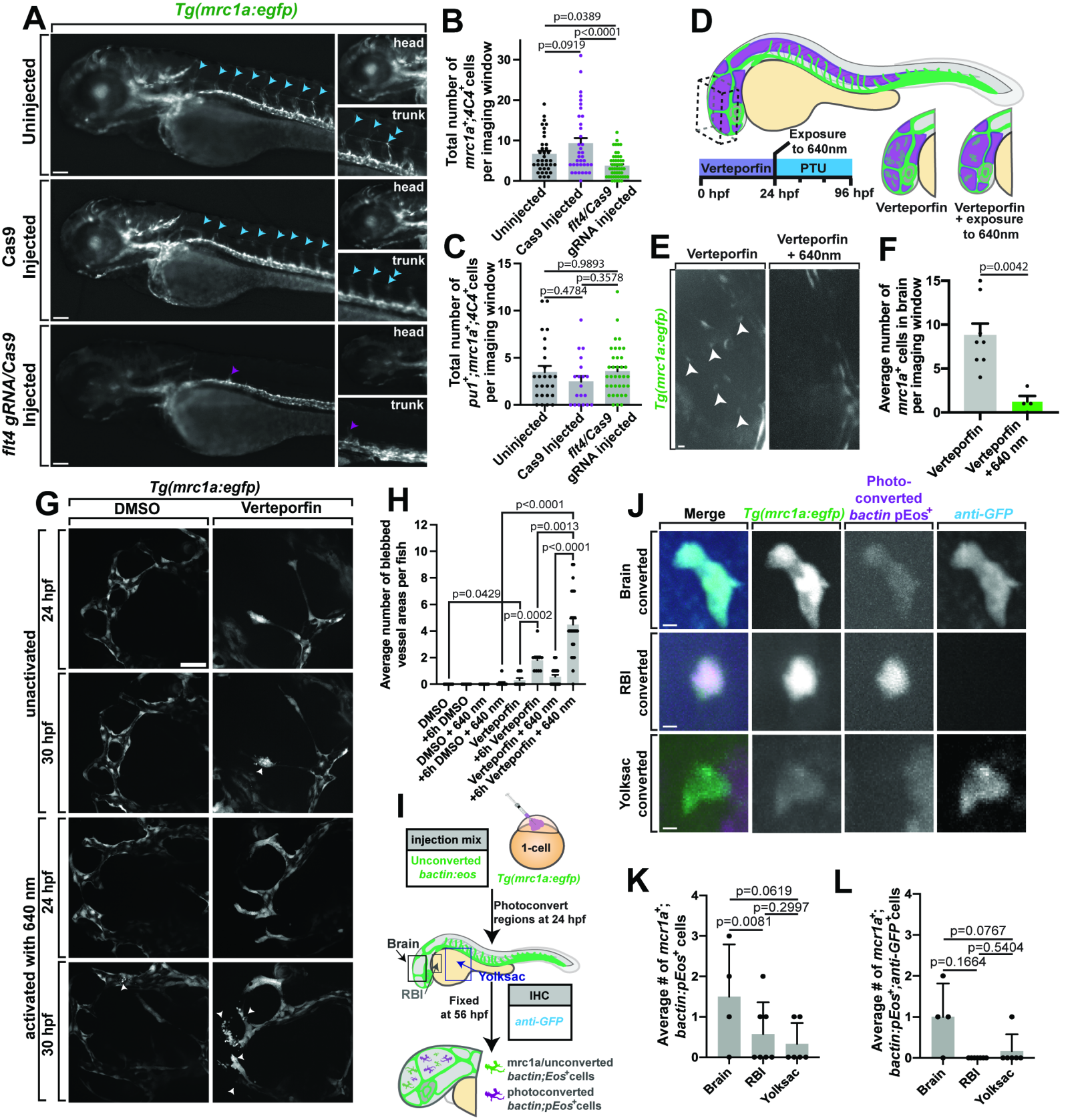
A
Tg(mrc1a:egfp)
Uninjected
Cas9 Injected
flt4 gRNA/Cas9 Injected
head
trunk
B
Total number of mrc1a+;4C4+ cells per imaging window
p=0.0389
p<0.0001
p=0.0919
Uninjected
Cas9 Injected
flt4/Cas9 gRNA injected
C
Total number of pu1+;mrc1a+;4C4+ cells per imaging window
p=0.9893
p=0.3578
p=0.4784
D
Exposure to 640nm
Verteporfin
PTU
0 hpf
24 hpf
96 hpf
Verteporfin
Verteporfin + exposure to 640nm
E
Verteporfin
Verteporfin + 640nm
Tg(mrc1a:egfp)
F
Average number of mrc1a+ cells in brain per imaging window
p=0.0042
Verteporfin
Verteporfin +640 nm
G
Tg(mrc1a:egfp)
DMSO
Verteporfin
unactivated
activated with 640 nm
24 hpf
30 hpf
H
Average number of blebbed vessel areas per fish
p<0.0001
p=0.0013
p<0.0001
p=0.0429
p=0.0002
DMSO
+6h DMSO
DMSO + 640 nm
+6h DMSO + 640 nm
Verteporfin
+6h Verteporfin
Verteporfin + 640 nm
+6h Verteporfin + 640 nm
I
injection mix
Unconverted bactin:eos
1-cell
Tg(mrc1a:egfp)
Photoconvert regions at 24 hpf
Brain
RBI
Yolksac
Fixed at 56 hpf
IHC
anti-GFP
mrc1a/unconverted bactin;Eos+cells
photoconverted bactin;pEos+cells
J
Merge
Tg(mrc1a:egfp)
Photo-converted bactin pEos+
anti-GFP
Brain converted
RBI converted
Yolksac converted
K
Average # of mrc1a+; bactin:pEos+ cells
p=0.0619
p=0.2997
p=0.0081
Brain
RBI
Yolksac
L
Average # of mrc1a+; bactin:pEos+;anti-GFP+ cells
p=0.0767
p=0.5404
p=0.1664
Brain
RBI
Yolksac

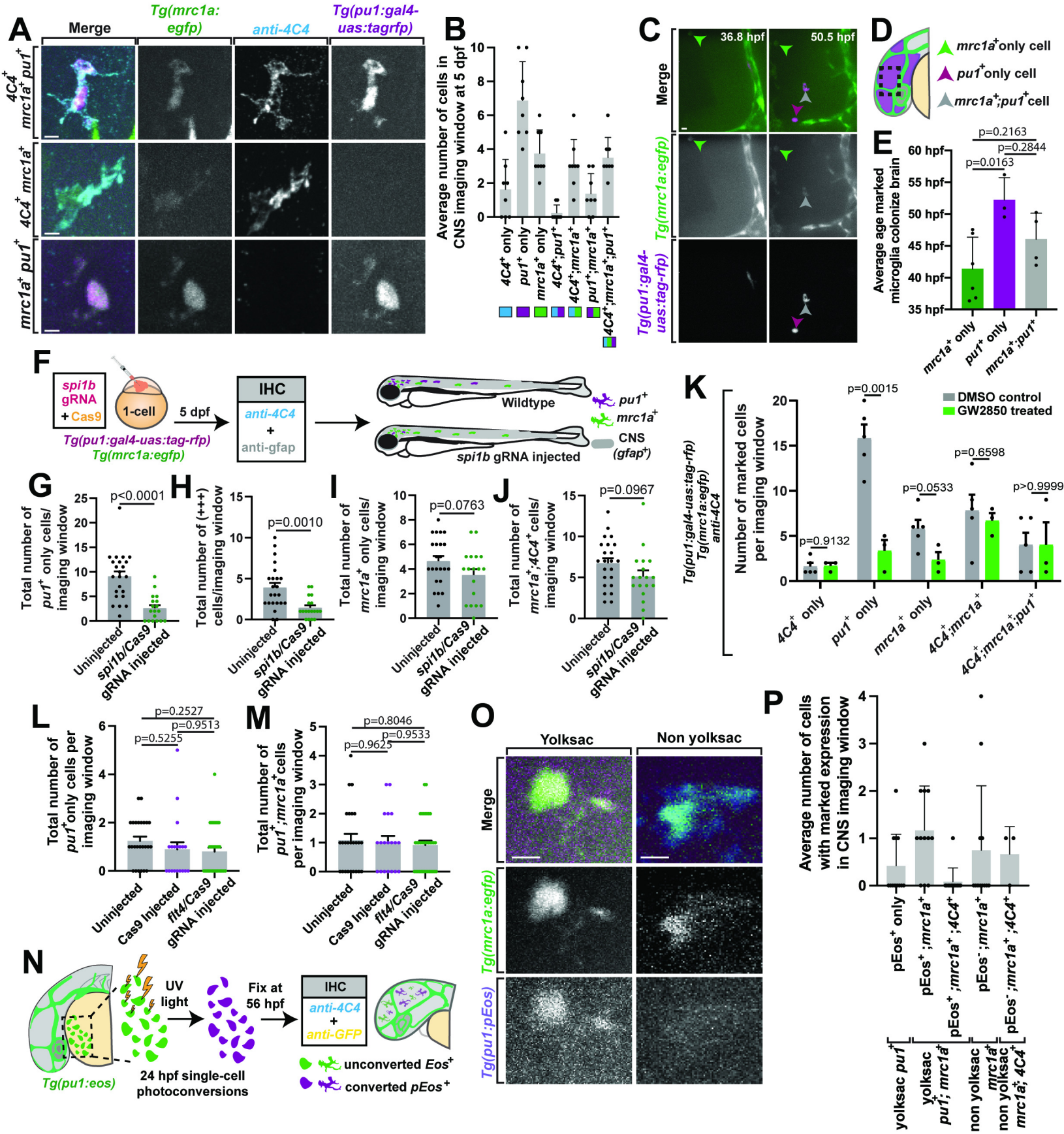
A
Merge
Tg(mrc1a:egfp)
anti-4C4
Tg(pu1:gal4-uas:tagrfp)
4C4+ mrc1a+ pu1+
4C4+ mrc1a+
mrc1a+ pu1+
B
Average number of cells in CNS imaging window at 5 dpf
4C4+ only
pu1+ only
mrc1a+ only
4C4+;pu1+
4C4+;mrc1a+
pu1+;mrc1a+
4C4+;mrc1a+;pu1+
C
36.8 hpf
50.5 hpf
Merge
Tg(mrc1a:egfp)
Tg(pu1:gal4-uas:tag-rfp)
D
mrc1a+only cell
pu1+only cell
mrc1a+;pu1+cell
E
Average age marked microglia colonize brain
p=0.2163
p=0.2844
p=0.0163
60 hpf
55 hpf
50 hpf
45 hpf
40 hpf
35 hpf
mrc1a+ only
pu1+ only
mrc1a+;pu1+
F
spi1b gRNA + Cas9
1-cell
5 dpf
IHC
anti-4C4 + anti-gfap
Tg(pu1:gal4-uas:tag-rfp)
Tg(mrc1a:egfp)
Wildtype
spi1b gRNA injected
pu1+
mrc1a+
CNS (gfap+)
G
Total number of pu1+ only cells/ imaging window
p<0.0001
Uninjected
spi1b/Cas9 gRNA injected
H
Total number of (+++) cells/imaging window
p=0.0010
I
Total number of mrc1a+ only cells/ imaging window
p=0.0763
J
Total number of mrc1a+;4C4+cells/ imaging window
p=0.0967
K
Tg(pu1:gal4-uas:tag-rfp) Tg(mrc1a:egfp) anti-4C4
Number of marked cells per imaging window
DMSO control
GW2850 treated
p=0.0015
p=0.9132
p=0.0533
p=0.6598
p>0.9999
4C4+ only
pu1+ only
mrc1a+ only
4C4+;mrc1a+
4C4+;mrc1a+;pu1+
L
Total number of pu1+only cells per imaging window
p=0.2527
p=0.9513
p=0.5255
Uninjected
Cas9 Injected
flt4/Cas9 gRNA injected
M
Total number of pu1+;mrc1a+cells per imaging window
p=0.8046
p=0.9533
p=0.9625
N
UV light
Fix at 56 hpf
IHC
anti-4C4 + anti-GFP
Tg(pu1:eos)
24 hpf single-cell photoconversions
unconverted Eos+
converted pEos+
O
Yolksac
Non yolksac
Merge
Tg(mrc1a:egfp)
Tg(pu1:pEos)
P
Average number of cells with marked expression in CNS imaging window
pEos+ only
pEos+;mrc1a+
pEos+;mrc1a+;4C4+
pEos-;mrc1a+
pEos-;mrc1a+;4C4+
yolksac pu1+
yolksac pu1+;mrc1a+
non yolksac mrc1a+
non yolksac mrc1a+;4C4+

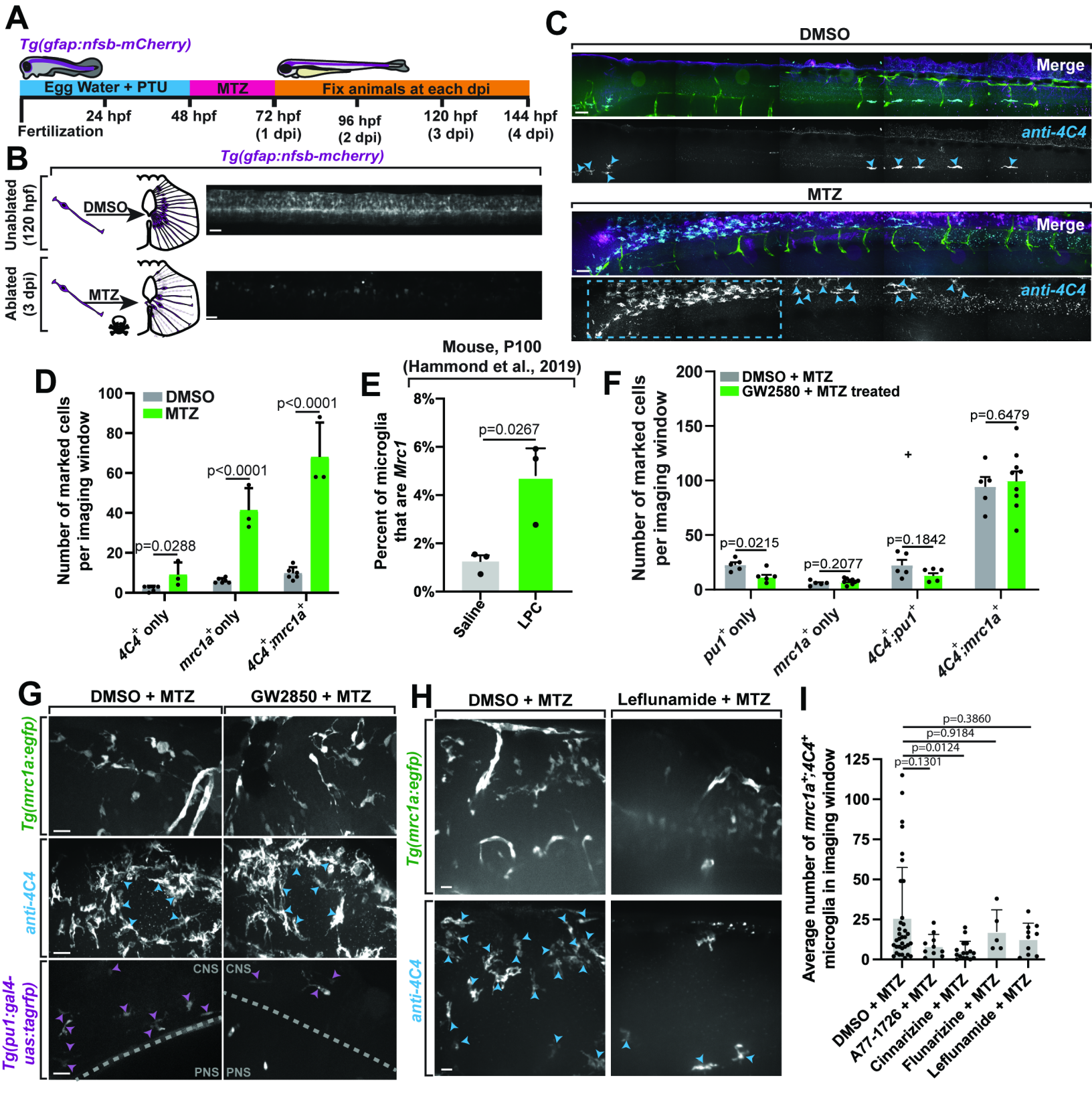
A
Tg(gfap:nfsb-mCherry)
Egg Water + PTU
MTZ
Fix animals at each dpi
Fertilization
24 hpf
48 hpf
72 hpf (1 dpi)
96 hpf (2 dpi)
120 hpf (3 dpi)
144 hpf (4 dpi)
B
Tg(gfap:nfsb-mcherry)
Unablated (120 hpf)
Ablated (3 dpi)
DMSO
MTZ
C
DMSO
MTZ
Merge
anti-4C4
D
Number of marked cells per imaging window
DMSO
MTZ
p=0.0288
p<0.0001
p<0.0001
4C4+ only
mrc1a+ only
4C4+;mrc1a+
E
Mouse, P100 (Hammond et al., 2019)
Percent of microglia that are Mrc1
p=0.0267
Saline
LPC
F
Number of marked cells per imaging window
DMSO + MTZ
GW2580 + MTZ treated
p=0.0215
p=0.2077
p=0.1842
p=0.6479
pu1+ only
mrc1a+ only
4C4+;pu1+
4C4+;mrc1a+
G
DMSO + MTZ
GW2850 + MTZ
Tg(mrc1a:egfp)
anti-4C4
Tg(pu1:gal4-uas:tagrfp)
CNS
PNS
H
DMSO + MTZ
Leflunamide + MTZ
Tg(mrc1a:egfp)
anti-4C4
I
Average number of mrc1a+;4C4+ microglia in imaging window
p=0.3860
p=0.9184
p=0.0124
p=0.1301
DMSO + MTZ
A77-1726 + MTZ
Cinnarizine + MTZ
Flunarizine + MTZ
Leflunamide + MTZ